PHYSICAL REVIEW B **94**, 115408 (2016)

Dynamics of the metal-insulator transition of donor-doped $SrTiO_3$

René Meyer,[1,2] Alexander F. Zurhelle,[1] Roger A. De Souza,[3] Rainer Waser,[1,4] and Felix Gunkel[1]
[1]*RWTH Aachen University, Institute of Electronic Materials (IWE 2) and Jülich Aachen Research Alliance - Fundamentals of Future Information Technology (JARA-FIT), 52056 Aachen, Germany*
[2]*Department of Materials Sciences and Engineering, Stanford University, Stanford, California 94305, USA*
[3]*RWTH Aachen University, Institute of Physical Chemistry (IPC) and JARA-FIT, 52056 Aachen, Germany*
[4]*Forschungszentrum Jülich, Peter Grünberg Institut (PGI-7) and JARA-FIT, 52425 Jülich, Germany*
(Received 3 May 2016; revised manuscript received 27 July 2016; published 6 September 2016)

The electrical properties of donor-doped $SrTiO_3$ (*n*-STO) are profoundly affected by an oxidation-induced metal-insulator transition (MIT). Here we employ dynamical numerical simulations to examine the high-temperature MIT of *n*-STO over a large range of time and length scales. The simulations are based on the Nernst-Planck equations, the continuity equations, and the Poisson equation, in combination with surface lattice disorder equilibria serving as time-dependent boundary conditions. The simulations reveal that *n*-STO, upon oxidation, develops a *kinetic* space charge region (SCR) in the near-surface region. The surface concentrations of the variously mobile defects (electrons, Sr vacancies, and O vacancies) are found to vary over time and to differ considerably from the values of the new equilibrium. The formation of the SCR in which electrons are strongly depleted occurs within nanoseconds, i.e., it yields a fast MIT in the near-surface region during the oxidation process. As a result of charge (over-)compensation by Sr vacancies incorporated at the surface of *n*-STO, this SCR is much more pronounced than conventionally expected. In addition, we find an anomalous increase of O vacancy concentration at the surface upon oxidation caused by the SCR. Our simulations show that the SCR fades in the long term as a result of the slow in-diffusion of Sr vacancies. We discuss implications for the electrical conductivity of *n*-STO crystals used as substrates for epitaxial oxide thin films, of *n*-STO thin films and interfaces, and of polycrystalline *n*-STO with various functionalities.

DOI: 10.1103/PhysRevB.94.115408

I. INTRODUCTION

Perovskite-type oxides exhibit a plethora of fascinating electronic material properties covering an exceptionally wide range of phenomena in solid state and surface physics [1,2]. The prototypical perovskite $SrTiO_3$ (STO), its isostructural cousin $BaTiO_3$ (BTO), and their solid solutions belong to the most widely studied oxides because of their diverse functionalities, including tunable high-*k* dielectric and electro-optical behavior, ferro- and piezoelectricity, and ionic conduction and photocatalytic activity. Layered in an atomically defined manner as epitaxial heterostructures and superlattices, material properties can be combined on the nanoscale level [3], and new functionality even can be generated at interfaces [1,4–6], making the family of perovskite oxides even more important and fascinating both for fundamental research and for technological applications.

STO is a d^0 band insulator with a band gap of 3.2 eV at 0 K. The valence band corresponds mainly to O 2*p* states, while the conduction band originates mainly from Ti 3*d* states [7]. Similar to semiconductors, many electronic phenomena in STO and BTO are induced or modified by doping. Donor doping through substitutions with higher valent cations, such as La^{3+} on Sr^{2+} sites or Nb^{5+} on Ti^{4+} sites, plays a particularly important role, because it generates electrons in STO. Therefore, after high-temperature fabrication of such donor-doped samples, the positive charges of ionized donors are balanced by an equal amount of electrons [Fig. 1(a)]. Because of STO's high permittivity, the energy levels of these hydrogenlike donors are very shallow, rendering donor-doped STO (*n*-STO) a degenerate, metallike semiconductor without carrier freeze-out, even at very low donor concentrations [8]. With the exception of very low temperatures, electron mobility is limited by phonon scattering with a room temperature value of approx. $6\,cm^2\,V^{-1}\,s^{-1}$ [9–15]. In contact with a high-work-function metal electrode, Schottky barriers are formed in *n*-STO due to the mismatch of the materials' work functions (e.g., Nb:STO/Au) [16–20].

n-STO is explored for functionalities as diverse as thermoelectricity [21–23], memristive switching [24–26], superconductivity [27,28], and photoelectrolysis [18,29]. In particular for the resistive switching behavior, the underlying physical mechanisms in devices based on *n*-STO are not understood in detail, and contradicting interpretations are under debate [25,30–34]. Furthermore, polycrystalline *n*-STO and donor-doped BTO (*n*-BTO) have been used commercially for decades in electronic components that functionalize oxidized grain boundaries as internal interfaces [35].

In addition to these direct functionalities, single crystalline *n*-STO is of great significance as a substrate for the epitaxial growth of oxide thin-film structures. It is the only electronically conducting perovskite that is commercially available as a substrate and is commonly used as a conducting (quasi-metallic) bottom electrode in epitaxial oxide electronic thin-film devices, such as resistively switching memories [36–38], ferroelectric tunnel junctions [39], or magnetic tunnel junctions [40]. While these novel device concepts often exploit advanced physical models, there is still a lack of understanding of some of the fundamental properties of the involved materials—in particular of the substrate, *n*-STO.

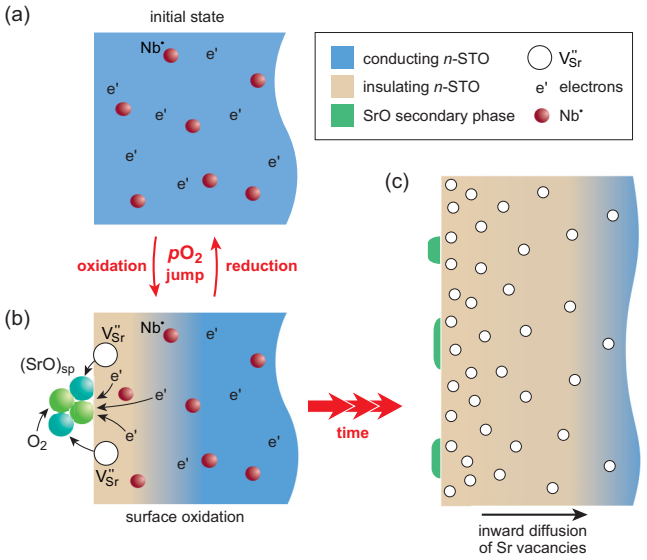

FIG. 1. Simplified sketch of the oxidation-induced metal-insulator transition of donor-doped $SrTiO_3$. In the initial state (a), the positive Nb donor charges ($Nb^{\cdot}$) are balanced by electrons (e'). Upon oxidation, the oxygen from the gas phase gets reduced by the free electrons in the near-surface region (a,b). Together with Sr ions from the topmost surface, nuclei of a SrO secondary phase are formed (leaving Sr vacancies behind). In this paper, we discuss an unexpected and significant "overoxidation" of the surface in the initial time regime, the formation of a correspondingly enhanced space charge region, and, in the long term, the diffusion of Sr vacancies into the bulk under time- and position-variable ambipolar acceleration (b,c). At the end of the process, the positive charge of ionized Nb dopants is balanced ionically by Sr vacancies, effectively acting as intrinsic codopants (*ionic charge balance*). In that case, *n*-STO turns into an insulating state. Note that the Kröger-Vink notation [52] is used in this sketch.

On the one hand, in physical models of thin-film devices, *n*-STO is commonly treated as a simple, metallic bottom electrode, in which the Fermi level is located close to or within the conduction band across the entire sample, all the way to the surface. At most, the formation of a Schottky barrier is considered for *n*-STO in contact with high-work-function metals. In this case, a space charge layer of purely *electronic* origin forms.

On the other hand, it has been known for a long time that *n*-STO (and *n*-BTO) may undergo an oxidation-induced metal-insulator transition (MIT) at high temperatures driven by the formation of cation vacancies. This process is generally regarded as a very slow process because of the very low diffusivities of the cation vacancies involved in this process. For this reason, the process is often neglected during the annealing of epitaxial films on *n*-STO at moderate temperatures. There are, however, clear indications that the oxidation-induced MIT is greatly accelerated at the surface and in the near surface layer of *n*-STO crystals, as will be discussed in more detail below. This oxidation-induced MIT leads to considerable changes in the *ionic* constitution of the surface of *n*-STO (or of the interface between a functional layer and a *n*-STO substrate), and these changes may drastically affect the electronic properties of the entire stack, as will be discussed in this paper.

Electrical charge neutrality in doped STO is generally explained by a lattice disorder model that determines the bulk concentration of native defects formed in STO as a function of thermodynamic boundary conditions. In the case of *donor*-doped STO, the excess *positive* charge of donors can be balanced *either* by electrons *or* by acceptor-type Sr vacancies depending on the ambient oxygen activity at high temperatures [41]. As a result, *n*-STO shows significant electronic conduction when annealed and quenched in moderately low oxygen pressures, but it undergoes a MIT, when the donor charge is compensated exclusively by Sr vacancies. In contrast, oxygen vacancies, as minority charge carriers, are widely regarded as less important in determining the bulk electronic properties of *n*-STO.

While the *thermodynamics* of the lattice disorder of *n*-STO in equilibrium are reasonably well understood [41,42], the *kinetics* of the high-temperature equilibration process and the corresponding MIT are yet to be elucidated in detail (Fig. 1). One main reason for the lack of understanding may be the extremely low diffusivity of Sr vacancies compared with that of O vacancies, with a difference of approximately 10 orders of magnitude at 1000 K [43]. As a consequence, the times for equilibration on macroscopic length scales are expected to be much larger for *n*-STO (governed by slow Sr diffusion kinetics) than for acceptor-doped STO (governed by O diffusion kinetics [44]).

While this behavior has been confirmed for macroscopic STO crystals [45,46], there is experimental evidence that appears to contradict the sluggish motion of Sr vacancies at and near the surface of *n*-STO. Kinetic studies of porous *n*-STO ceramics at $T \approx 1100$ K revealed fast electrical response times for both oxidation and reduction processes comparable to those found in acceptor-doped STO [47]. The nanoionic resistive switching of donor-doped STO mentioned above also has been found, surprisingly, to occur at the same rate as that of undoped and acceptor-doped STO [33]. Moreover, the *n*-type conducting interface between $LaAlO_3$ and $SrTiO_3$ shows the typical ionic compensation behavior of *n*-STO under oxidizing conditions already at $T \approx 1000$ K [48,49], indicating rather rapid migration kinetics of the cation sublattice of STO on nanometer length scales.

The present paper discusses in detail a transport model that describes quantitatively all the significant features of the oxidation-induced MIT over a dynamic range in time, spanning more than 18 orders of magnitude. In a previous paper, we examined the long-time behavior of the MIT using ^{18}O tracer diffusion experiments, and we proposed a transport model that accounted for the observed behavior [46]. Here, we provide a comprehensive description of the MIT on the short, intermediate, and long time scales. This transport model allows us to elucidate the origin of the apparent contradictions (referred to above) regarding the fast electrical response of porous ceramics and of resistive switches, as well as the defect dynamics of complex oxide interfaces. It also allows us to predict the behavior of *n*-STO substrates at conditions relevant to the growth and annealing of thin films and substrates. Indeed, our results emphasize that oxygenating deposited films, in order to achieve optimal film functionalities, may

deleteriously affect the required functionality (conductivity) of the substrate.

II. FUNDAMENTALS AND COMPUTATIONAL METHODOLOGY

A. Fundamentals of the lattice disorder in donor-doped STO

Over the last decades, the bulk lattice disorder of STO (and of isostructural BTO) as a model perovskite-type oxide has been studied extensively. The equilibrium thermodynamics of lattice disorder in these materials, acting as the basis for our dynamic study, is reviewed in this section. Because we performed our study on STO, we will focus on STO, although most of the conclusions hold for BTO in good approximation, too, as the material properties of BTO are only slightly different. Where appropriate, we will refer to studies on BTO for completeness.

Please note that in classical semiconductors such as Si doped with donors, the charge neutrality is maintained through a balance of ionized donors and electrons. Counterdoping by acceptors leads to compensation of the donors and a corresponding decrease of the electron concentration. In metal oxides, such as the STO discussed here, these compensating acceptors may arise from the incorporation of native ionic defects. The balance between *electronic charge carriers* (electrons and holes), *charged dopants*, and *charged native defects* (oxygen vacancies and cation vacancies, in particular Sr vacancies) controlled by means of thermodynamic boundary conditions (temperature and oxygen pressure) is at the heart of the lattice disorder model of STO and of the observed oxidation-induced MIT.

1. Intrinsic defect formation processes in STO

During the growth of single crystals and the sintering of polycrystals at very high temperatures ($T > 1800$ K), cation and anion vacancies are formed through Schottky disorder. Interstitial defects can be neglected even at these high temperatures. In fact, their formation energies are extremely high because of the high packing density of the ABO_3 perovskite lattice [43,50]. In the case of STO, O vacancies and Sr vacancies are formed, while Ti vacancies are less likely because their formation is energetically more costly [47,51].

At these high temperatures, STO establishes a Schottky equilibrium [Eq. (1), top], with defect concentrations according to the corresponding law of mass action [Eq. (1), bottom]

$$\mathrm{Sr}_{\mathrm{Sr}}^{x} + \mathrm{O}_{\mathrm{O}}^{x} \rightleftarrows \mathrm{V}_{\mathrm{Sr}}'' + \mathrm{V}_{\mathrm{O}}^{\cdot\cdot} + (\mathrm{SrO})_{\mathrm{s.p.}}$$
$$K_{\mathrm{S}}(T) = \left[\mathrm{V}_{\mathrm{Sr}}''\right] \cdot \left[\mathrm{V}_{\mathrm{O}}^{\cdot\cdot}\right] \quad (1)$$

Here we use the Kröger-Vink notation for point defects in the crystal lattice [52]. $\mathrm{Sr}_{\mathrm{Sr}}^{x}$ and $\mathrm{O}_{\mathrm{O}}^{x}$ are ions on regular sites of the Sr and O sublattices. $\mathrm{V}_{\mathrm{O}}^{\cdot\cdot}$ and $\mathrm{V}_{\mathrm{Sr}}''$ denote O vacancies and Sr vacancies, doubly positively and negatively ionized, respectively, relative to the regular crystal lattice. $(\mathrm{SrO})_{\mathrm{s.p.}}$ represents the secondary phase, which is formed at external or internal interfaces (i.e., surfaces or grain boundaries) of the crystal as a result of mass conservation [53,54]. Because of this process, the formation of Sr vacancies occurs *at* surfaces or interfaces [Fig. 1(b)]. Equilibration of the entire system is then mediated by the diffusion of defects into the bulk [Fig. 1(c)]. As a separate phase, SrO has a constant activity and, therefore, does not appear in the mass action equation. $K_{\mathrm{S}}(T)$ denotes the reaction constant of the Schottky equilibrium. (Note that it remains to be elucidated how this thermodynamically controlled reaction at the surface of STO relates atomistically to the surface reconstruction and the $\mathrm{Ti}_n\mathrm{O}_m$ structures observed by scanning tunneling microscopy on the surfaces of n-STO crystals [55–57].)

To establish the Schottky equilibrium [Eq. (1)] on a reasonable time scale, the diffusion of the vacancies has to be fast. The self-diffusion coefficients $\mathrm{V}_{\mathrm{O}}^{\cdot\cdot}$ and $\mathrm{V}_{\mathrm{Sr}}''$ in STO have been studied extensively by various experimental techniques and by simulation. It turns out that O vacancies show high mobility in the perovskite lattice and a low activation energy of diffusion of 0.6–1.0 eV [58,59]. In contrast, Sr vacancies exhibit very low mobility and a high activation energy of 2.5–4.0 eV [43,46]. A compilation of data from selected literature is provided in Supplemental Material Fig. S1 [60]. As we shall see, the huge differences in the self-diffusion coefficients of $\mathrm{V}_{\mathrm{O}}^{\cdot\cdot}$ and $\mathrm{V}_{\mathrm{Sr}}''$ have a tremendous impact on the lattice disorder of n-STO during the oxidation process and the oxidation-induced dynamics of the MIT. Because of the very low mobility of $\mathrm{V}_{\mathrm{Sr}}''$, the Schottky equilibrium [Eq. (1)] is only approached within reasonable times in the high-temperature (HT) regime, i.e., approximately $T > 1300$ K, in macroscopic crystals (micrometer sizes and larger).

The density of oxygen vacancies $[\mathrm{V}_{\mathrm{O}}^{\cdot\cdot}]$ is coupled to the ambient atmosphere as described by the oxygen exchange equilibrium

$$\mathrm{O}_{\mathrm{O}} \rightleftarrows \mathrm{V}_{\mathrm{O}}^{\cdot\cdot} + 2e' + \tfrac{1}{2}\mathrm{O}_2(\mathrm{g})$$
$$K_{\mathrm{O}}(T) = [\mathrm{V}_{\mathrm{O}}^{\cdot\cdot}] \cdot n^2 \cdot p\mathrm{O}_2^{0.5}, \quad (2)$$

reflecting the removal of oxygen from the lattice into the gas phase. As a consequence, O vacancies and electrons are generated in the perovskite lattice. $K_{\mathrm{O}}(T)$ denotes the temperature-dependent mass action coefficient for the reduction reaction of the oxygen sublattice.

Because of the high mobility of O vacancies, Eq. (2) of the oxygen sublattice is active on macroscopic length scales down to moderate temperatures (MT regime). It has a lower temperature limit of approximately 500–700 K. Contrary to common assumptions, this limit is not at all due to the mobility of the O vacancies being too low (it is small but still significant at even lower temperature), but because the *kinetics* of the exchange reaction (2) at the surface become too sluggish [61,62].

At low temperatures (LT regime) down to 0 K, only the electronic equilibrium

$$\emptyset \rightleftarrows \mathrm{e}' + \mathrm{h}^{\cdot}$$
$$K_e(T) = n \cdot p \quad (3)$$

remains active. The temperature dependence of the reaction constant K_{e} is related to the band gap, in analogy to classical semiconductor physics (see Table I).

2. Doping in STO

During fabrication, foreign cations can be substitutionally incorporated as dopants to control both the defect structure and the electronic properties of STO. Cation substitutions with lower valent cations (e.g., Al or Fe on Ti sites) lead

TABLE I. Mass action laws determining the bulk defect chemistry of n-STO, as well as important material parameters such as self-diffusion coefficients, electron mobility, dielectric constant, and band gap, collected from the literature (Ref. [76]). The temperature dependence is given in the center column. On the right-hand side, the values have been evaluated for a temperature of 1500 K, which were chosen for our model calculations.

Material constants in $SrTiO_3$					
Constant				Value at $T = 1500\,\mathrm{K}$	Ref.
Band gap	$E_g(T)$	$3.17 - 5.66 \times 10^{-4} \times T/K$	[eV]	2.32 eV	[41]
Electronic equilibrium	$K_e(T)$	$1.43 \times 10^{33} \times (\frac{T}{\mathrm{K}})^3 \exp(-\frac{E_g}{k_B T})$	$[\frac{1}{\mathrm{cm}^6}]$	$7.74 \times 10^{34}\ \frac{1}{\mathrm{cm}^6}$	[41]
Oxygen exchange equilibrium	$K_O(T)$	$5 \times 10^{71} \times \exp(-\frac{6.1\,\mathrm{eV}}{k_B T})$	$[\frac{\mathrm{bar}^{0.5}}{\mathrm{cm}^9}]$	$1.60 \times 10^{51}\ \frac{\mathrm{bar}^{0.5}}{\mathrm{cm}^9}$	[41]
Schottky equilibrium	$K_S(T)$	$3 \times 10^{44} \times \exp(-\frac{2.5\,\mathrm{eV}}{k_B T})$	$[\frac{1}{\mathrm{cm}^6}]$	$1.20 \times 10^{36}\ \frac{1}{\mathrm{cm}^6}$	[41]
High-temperature redox equilibrium	$K_R(T) = K_S/K_O$	$6 \times 10^{-28} \times \exp(+\frac{3.6\,\mathrm{eV}}{k_B T})$	$[\frac{\mathrm{cm}^3}{\mathrm{bar}^{0.5}}]$	$7.48 \times 10^{-16}\ \frac{\mathrm{cm}^3}{\mathrm{bar}^{0.5}}$	
Electron mobility	$\mu_n(T)$	$3.95 \times 10^4 \times (T/\mathrm{K})^{-1.62}$	$[\frac{\mathrm{cm}^2}{\mathrm{Vs}}]$	$0.28\,\frac{\mathrm{cm}^2}{\mathrm{Vs}}$	[41]
Self-diffusion coefficient for oxygen vacancies	$D_{V_O^{\cdot\cdot}}(T)$	$0.33 \times \exp(-\frac{1.0\,\mathrm{eV}}{k_B T})$	$[\frac{\mathrm{cm}^2}{\mathrm{s}}]$	$1.44 \times 10^{-4}\ \frac{\mathrm{cm}^2}{\mathrm{s}}$	[67]
Self-diffusion coefficient for Sr vacancies	$D_{V''_{Sr}}(T)$	$5 \times 10^{-5} \times \exp(-\frac{2.8\,\mathrm{eV}}{k_B T})$	$[\frac{\mathrm{cm}^2}{\mathrm{s}}]$	$1.96 \times 10^{-14}\ \frac{\mathrm{cm}^2}{\mathrm{s}}$	[103]
Dielectric constant	$\varepsilon_r(T)$	$\frac{78400}{(T/\mathrm{K})-28}$		53.2	[104]

to an acceptor doping of the STO lattice. The acceptor energy levels always lie deep in the band gap of STO [63]. As a consequence, the negatively charged ionized acceptors are preferably compensated *ionically* by the incorporation of positively charged oxygen vacancies, while holes are always minority carriers. It is important to note that Sr vacancies, incorporated in the HT regime [Eq. (1)], also act as (native) acceptors. Because of this, even ideally undoped STO will act as slightly acceptor-doped, too. As noted previously, the thermodynamics and the kinetics of the lattice disorder of such an acceptor-doped STO have been comprehensively studied and are well understood, both in the bulk [10,42,61,64–68] as well as in thin films [69] and near-surface space charge regions [58,70,71].

Higher valent cation substitutions, such as La on Sr sites ($La_{Sr}^{\cdot}$) or Nb on Ti sites ($Nb_{Ti}^{\cdot}$), establish extrinsic donor centers in the STO lattice. Due to the shallow energy levels, the donors can be charge balanced by electrons. However, as mentioned above, donors also can be compensated by Sr vacancies V''_{Sr}. Because of these two different charge balance mechanisms for n-STO, the thermodynamics of the lattice disorder of *donor*-doped STO is very different from that of *acceptor*-doped STO (see, e.g., [46,72–74] and a comprehensive paper by Moos and Härdtl [41]). In particular, the dominant charge balance mechanism in n-STO may change with ambient atmosphere, as discussed in the following section.

3. *Equilibrium defect concentrations and mixed ionic-electronic charge balance in n-STO*

Based on the mass action constants of the defect equilibria [Eqs. (1)–(3)] and the dopant densities introduced during fabrication of the crystal, all majority and minority densities can be calculated as a function of the oxygen partial pressure (pO_2) and T using the charge balance [electroneutrality (EN)] condition. For donor-doped STO, the EN condition reads

$$2[V_O^{\cdot\cdot}] + [D^{\cdot}] - 2[V''_{Sr}] - n = 0, \tag{4}$$

where $[D^{\cdot}]$ denotes the density of the donors. Here, we can neglect the fact that O vacancies can be singly charged because their concentration is negligible at the temperatures considered here [75]. This simplification does not affect the general validity of the lattice disorder model [41].

Figure 2(a) shows the resulting HT equilibrium concentrations for 1 at % donor-doped STO at an exemplary temperature of 1500 K as a function of pO_2 using the material constants listed in Table I [76]. At $T = 1500\,\mathrm{K}$, all defect equilibria [Eqs. (1)–(3)] are active. For convenience, we will keep this temperature throughout this paper for the discussion of the equilibration dynamics. The dopant concentration is typical for Nb:STO substrates used for thin-film synthesis, as well as for functional ceramic devices.

Three pO_2 regimes can be distinguished. In very reducing atmospheres ($pO_2 < 10^{-15}$ Pa), the majority carriers are O vacancies, and their charge is balanced by electrons, $n \approx 2[V_O^{\cdot\cdot}]$ [Fig. 2(a), light blue area]. In moderately reducing atmospheres (approximately $10^{-15}\,\mathrm{Pa} < pO_2 < 10^{-5}\,\mathrm{Pa}$), the donors and electrons are majority carriers (red area). Hence, in approximation, the EN condition is given by electrons balancing the charge of the ionized donors $n \approx [D^{\cdot}]$ (pO_2 regime of *electronic charge balance*).

In oxidizing atmospheres ($pO_2 > 10^{-5}$ Pa), the donors and Sr vacancies, increasingly formed upon oxidation [cf. Eq. (1)], are majority carriers (green area). Here, the EN condition is given by the negative charge of Sr vacancies compensating the positive charge of donors $[D^{\cdot}] \approx 2[V''_{Sr}]$ (pO_2 regime of *cation vacancy charge balance,* also called *ionic compensation*). In this region, n drops below the donor concentration level. Unlike in semiconductors, the electron density in n-STO can thus be strongly reduced below the donor level, resulting in a low electronic conductivity and even insulating behavior when the ionized donors are compensated exclusively by ionic Sr vacancies.

The boundary between the two latter EN regimes shifts towards higher pO_2 with increasing temperature. Thus, ionic compensation is suppressed increasingly at higher

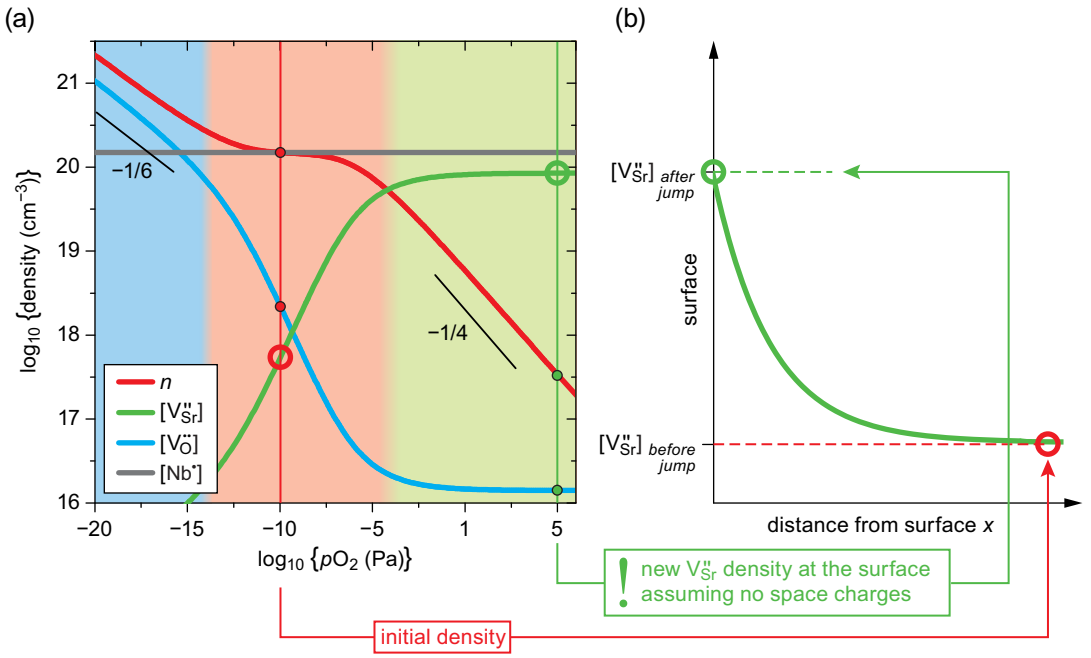

FIG. 2. Calculated densities of point defects for 1 at % donor-doped $SrTiO_3$ in the high-temperature (HT) regime. The concentrations of electrons, O vacancies, and Sr vacancies are shown as a function of the ambient oxygen partial pressure pO_2 for $T = 1500$ K. The material parameters are taken from Table I. (a) Equilibrium defect concentrations established after sufficiently long equilibration times. Three pO_2 regimes are indicated: intrinsic regime at extremely reducing conditions in which electrons and O vacancies constitute the majority defects (blue), the regime of electron charge balance in which $n \approx [D^{\cdot}]$ holds (red), and the regime of cation vacancy charge balance in which $2[V''_{Sr}] \approx [D^{\cdot}]$ is approached at very oxidizing conditions (green). (b) Sketch of an assumed concentration profile of Sr vacancies (least mobile particles) in the conventional (chemical diffusion) model after an (instantaneous) change of the pO_2 from the regime of electronic charge balance (10^{-10} Pa) to the regime of cation vacancy charge balance (10^5 Pa), see lines in panel (a). x shows the distance from the surface. The conventional model does not take into account the formation of space charges and the interaction of the point defects during the diffusion process.

temperatures (see Supplemental Material Fig. S2 [60]). For this reason, a donor-doped STO crystal grown in air at $T > 1800$ K is an electronically charge-balanced material that remains conducting.

An MIT is induced when the pO_2 is changed from the electron charge-balanced regime [red area in Fig. 2(a)] to the cation vacancy charge-balanced regime (green area) at a given temperature. As a result of the formation of Sr vacancies at the surface and their penetration into the crystal, SrO-rich secondary phases form during the oxidation process, as mentioned above [53,77,78].

To study the MIT in detail, it is most convenient to consider the so-called HT redox equilibrium one receives by combining Eqs. (1) and (2):

$$\mathrm{Sr}^{x}_{\mathrm{Sr}} + \frac{1}{2}\mathrm{O}_2(\mathrm{g}) + 2\mathrm{e}' \rightleftarrows \mathrm{V}''_{\mathrm{Sr}} + (\mathrm{SrO})_{\mathrm{s.p.}}$$

$$K_{\mathrm{R}}(T) = \frac{K_{\mathrm{S}}(T)}{K_{\mathrm{O}}(T)} = \frac{[\mathrm{V}''_{\mathrm{Sr}}]}{n^2 \cdot pO_2^{0.5}}. \quad (5)$$

To achieve controlled lattice disorder and n-type conducting doped STO single crystals, ceramics, and thin films, a suitable temperature (and gas atmosphere) treatment can be derived based on the equilibrium defect concentrations discussed above. Typically, this is done by a first anneal in the HT regime (where the Schottky equilibrium is active; setting a well-defined Sr vacancy concentration), a subsequent second anneal in the MT regime at a given pO_2 (to establish a well-defined O vacancy density), and a final quenching into the LT regime, in which the electronic equilibrium is established. Hence, a combination of *temperature* and *oxygen pressure* is chosen according to the bulk lattice order model.

As we will show, these different temperature regimes can also be mapped onto different time scales. A sudden change of the pO_2 for a micrometer-sized crystal at 1500 K will lead to

(i) a new electronic equilibrium within tens of *picoseconds* because of the high mobility of electrons,

(ii) a new equilibrium of the oxygen sublattice within *milliseconds* because of the moderately high mobility of O vacancies, and

(iii) a new Schottky equilibrium (i.e., equilibrium of the Sr sublattice) within *days* because of the very low mobility of Sr vacancies.

A justification of the time scales will be provided below. Figure 2(a) refers to time scale (iii); that is, it reflects the equilibrium of all electronic charge carriers and ionic sublattices.

B. Kinetics of the oxidation-mediated MIT—limitations of the classical approach

To address the dynamics of the high-temperature MIT in donor-doped STO, we consider a sudden jump in pO_2 from the regime of the electronically charge-balanced ionized

donors [Fig. 1(a)] to the regime of cation vacancy charge balance [Figs. 1(b,c)], which then drives the material into a new equilibrium of lattice disorder. Here, we specifically discuss a sudden jump from $pO_2 = 10^{-10}$ Pa (electronic charge balance) to $pO_2 = 10^5$ Pa (ionic charge balance) at $T = 1500$ K for $[D^{\cdot}] = 1$ at % [cf. Fig. 2(a)]. Hence, before the jump, the charge of ionized donors is balanced by electrons, while Sr vacancies and O vacancies are minority carriers. Upon the jump to $pO_2 = 10^5$ Pa, the surface concentration of the Sr vacancy concentration increases by several orders of magnitude, while the electron concentration drops accordingly [cf. new equilibrium at $pO_2 = 10^5$ Pa in Fig. 2(a)]. The O vacancy concentration is reduced.

In the classical approach, the jump in pO_2 leads to an immediate change of the concentrations at the surface according to Eq. (5), followed by the diffusion of point defects into the interior until the new equilibrium in ionic compensation is achieved throughout the bulk. The process rate for diffusion is assumed to be determined by the least mobile species—in our case, obviously the Sr vacancies. The classical approach considers local charge neutrality as well as time-independent boundary conditions during the process. Therefore, the oxidation process spreads into the interior of the STO crystal by the diffusion of Sr vacancies following Fick's second law. This yields an exponential concentration profile [Fig. 2(b)], because this process can be regarded as a diffusion from an infinite source. Based on the V''_{Sr} self-diffusion coefficient (Table I), a penetration depth of just a few nanometers would be expected for a diffusion time of some seconds (L_D ($t = 1$ s, 1500 K) $\approx$1 nm here, using $L_D^2 = D_{V''_{Sr}}(T) \cdot t$, where D_{def} is the self-diffusion coefficient of the defect 'def').

As mentioned in the Introduction and elaborated in more detail below, however, the short-term oxidation process is observed to occur many orders of magnitude faster than the classical approach suggests. The charge-neutral classical treatment of the diffusion process hence seems to be too simplified, and a substantial extension of the classical model is needed. As we shall see, the key to the improved understanding lies in the interaction of the defects during the MIT and the formation of a transient space charge region (SCR) near the surface having tremendous impact on the time evolution of the process. In particular, the associated electric field within the SCR, accelerating (decelerating) the dynamics of the oxidation process, needs to be considered.

C. Numerical model with time-variant boundary conditions

1. Space charge formation and related diffusion processes

For the diffusion of charged species, the electrostatic interaction of the defects with an internal electric field has to be considered. Internal drag fields naturally arise when charged defects move differently fast, leading to a separation of charge in the process. The resulting electric field accelerates slow species and decelerates fast species and, hence, couples the diffusion of all species. This is classically captured in the framework of *ambipolar* diffusion. The kinetics of diffusion of different species are then determined by the common ambipolar diffusion coefficient as already pointed out by Carl Wagner [79]. Since then, ambipolar diffusion is used as the textbook model for the entire area of semiconductor physics [80] and ionic crystals [81]. Typically, there are just two mobile defects to be considered, so that an analytical expression of the ambipolar diffusion coefficient of two charged species, A and B, can easily be derived [82,83] as

$$\tilde{D} = D_A D_B \cdot \frac{C_A + (z_A/z_B)^2 C_B}{D_A C_A + (z_A/z_B)^2 D_B C_B} \tag{6}$$

where D_i, C_i, and z_i are the self-diffusion coefficients, densities, and charge numbers of species A and B.

In our case, however, there are *three* charged species involved, electrons, Sr vacancies, and O vacancies. Although the case of three charge carriers has been considered in the literature [84,85], in our case, there is a further major complication: Electrons (Sr vacancies) change from being *majority* (*minority*) carriers to *minority* (*majority*) carriers in the course of the MIT process. As a consequence, an analytical solution is not feasible, and a numerical approach is called for. This approach is based on generic transport equations with the self-diffusion coefficients of all species combined with the reaction equations given in Section II A. It *implicitly* considers the (ambipolar) coupling of the diffusion coefficients of all involved species.

In the case of *n*-STO, the self-diffusion coefficients of electrons, Sr vacancies, and O vacancies differ by many orders of magnitude (cf. Supplemental Material Fig. S1 [60] and Table I). Thus, because of the high mobility (self-diffusion coefficient) of electrons, the equilibration process driven by the pO_2 jump illustrated in Fig. 2(a) immediately leads to the formation of a space charge ρ_{SC} and an electric field E according to the Poisson equation

$$\rho_{SC} = \frac{\partial}{\partial x}(\varepsilon_0 \varepsilon_r E). \tag{7}$$

The electric field E, also termed *Nernst* field, provides the ambipolar coupling of the species.

To accommodate the presence of a local space charge ρ_{SC} into our model, the local EN condition [Eq. (4)] is replaced by a more general charge balance equation including the local space charge ρ_{SC},

$$e_0\{2[V_O^{\cdot\cdot}](x) + [D^{\cdot}] - n(x) - 2[V''_{Sr}](x)\} = \rho_{SC}(x) \neq 0. \tag{8}$$

Here, x specifies the distance from the surface. The space charge ρ_{SC} has to be considered at the surface ($x = 0$) and in the entire near-surface region ($x > 0$) in which concentration gradients occur in the course of the pO_2-induced MIT process. In particular, it is the nonzero ρ_{SC} that mediates an electron depletion layer ahead of the Sr vacancy diffusion front, as will be shown below.

Instead of the *local* EN [Eq. (4)], a *global* electroneutrality condition, i.e., an overall charge balance, now serves as a conditional equation,

$$\int_0^\infty \rho_{SC}(x)dx \equiv 0. \tag{9}$$

Hence, while locally charge neutrality may be violated during the process, the overall system stays charge-neutral at any time.

It should be noted that the space charge only appears because of the pO_2 jump. Before the jump, the EN condition holds locally throughout the crystal [i.e., $\rho_{sc}(x) = 0$ everywhere in the crystal]. As we shall see, in our model, the space charge disappears again for very long times when the densities of all species have approached their new equilibrium values. For this reason, we speak about a *kinetic* or *transient space charge* which controls the time evolution of the MIT in donor-doped STO. This process thus differs from the equilibrium surface space charge layer found in acceptor-doped STO, which is driven by a lowered enthalpy of oxygen vacancy formation at the surface [58,70].

In the next section, we propose a numerical model, which considers both the variation of the surface and near-surface defect concentrations by local space charges and the concentration dependence of the diffusion coefficients inside the material. The model reflects, therefore, the mandatory expansion of classical approaches in order to understand the transient behavior of n-STO upon oxidation.

2. Model equations

Inside our model, we calculate the particle flux density j_i from the Nernst-Planck equation for each individual type of defect

$$j_i = -D_i \frac{\partial}{\partial x} C_i - \frac{z_i}{|z_i|} \mu_i C_i \frac{\partial}{\partial x} \varphi \quad i \in \{V_O^{\cdot\cdot}, V_{Sr}'', e'\}, \tag{10}$$

where φ denotes the inner electric potential. The gradient is taken with respect to the distance x from the surface. The first term on the right constitutes the diffusion term, and the second term is the drift term of the particle flux density, reflecting the fact that because of their charge, all involved species—electronic and ionic—are affected by an electric field. The diffusion coefficient D_i and the mobility μ_i of an ionic species i are linked by the Nernst-Einstein relationship.

To calculate the evolution of concentrations as a function of time, the continuity equation is applied,

$$\frac{\partial}{\partial t} C_i = -\frac{\partial}{\partial x} j_i. \tag{11}$$

In Eq. (11) we neglect source and sink terms for all species under consideration. This simplifies the calculation, and it is justified because of the following facts: The concentration of electrons is always significantly higher than the concentration of holes, i.e., $n \gg p$, for donor-doped STO in all pO_2 regimes [41], so that source and sink effects based on the generation and recombination of electrons and holes, Eq. (3), can be neglected. In the perovskite lattice, there are also no source and sink effects for the ionic species (only at the surface and, possibly, at internal interfaces, e.g., grain boundaries), because only vacancies have to be considered, while interstitials can be neglected in STO, as mentioned in Sec. II A. Moreover, the ionization state or valence state of ionic species remains unchanged during the process. That is, donors are always $D^{\cdot}$, Sr vacancies V_{Sr}'', and oxygen vacancies $V_O^{\cdot\cdot}$.

The electric field and the corresponding electrostatic potential distribution occurring in the course of the process and driving the ambipolar diffusion are calculated from Poisson's equation

$$\frac{\partial^2}{\partial x^2} \varphi = -\frac{\rho_{SC}}{\varepsilon_0 \varepsilon_r} \tag{12}$$

and Maxwell's first equation

$$E = -\frac{\partial}{\partial x} \varphi. \tag{13}$$

In our calculations, we assume the dielectric constant ε_r to depend on the temperature only [86]. For simplicity and due to a lack of experimental data, a dependency on the internal electric field [87] at high temperatures is not considered. (The effect is expected to be small in the cubic phase at high temperature [87].) The space charge distribution inside the model system is given by Eq. (8).

To compute the diffusion problem, three conditional equations serving as the boundary conditions at the surface have to be defined for electrons, oxygen vacancies, and cation vacancies. Two boundary conditions of the *Dirichlet* type are given by the law of mass actions of the surface defect reactions, based on Eqs. (5) and (2), respectively:

$$[V_{Sr}'']_{surf} = [V_{Sr}''](x = 0) = K_s(T) \cdot n_{surf}^2 \cdot pO_2^{0.5} \tag{14}$$

$$[V_O^{\cdot\cdot}]_{surf} = [V_O^{\cdot\cdot}](x = 0) = \frac{K_O(T)}{n_{surf}^2 \cdot pO_2^{0.5}} \tag{15}$$

The application of these boundary conditions implies that the kinetics of the surface defect reaction is *fast* compared with the diffusion kinetics. This is justified by the high temperatures used in our study ($T > 1000$ K) [88]. Thus, the local equilibrium at the surface can be presumed for all times. The surface concentration of electrons is involved in the surface mass actions laws (14,15). The last conditional equation needed to calculate the concentrations of all species is the global conservation of charge, introduced as Eq. (9). With the set of differential equations and the three conditional equations describing the boundary conditions for the free surface of donor-doped STO crystals, the system is fully determined.

3. Numerical model

An implicit finite-difference method is used to calculate the time-dependent concentration profiles, as well as the electric properties, i.e., the space charge profile, the electric field profile, and the electrostatic potential profile for a one-dimensional cut through the crystal. To obtain a better spatial resolution near the surface, flexible nonequidistant spatial slicing has been employed. The nonlinear set of equations consisting of the transport equations and the boundary conditions is solved by a multidimensional damped Newton algorithm. The implicit method makes it possible to obtain a stable solution for large time increments in the case of large differences in the diffusion coefficients of the particles involved. In fact, we were able to predict the kinetics of the MIT from 10^{-12} to $>10^6$ s, i.e., >18 decades in time [time steps were chosen logarithmically, with 10 time steps per decade, with $-12 < \log(t/s) < 6$]. Such a huge dynamic range is required because of the very different time scales of the

processes involved. For additional details about our numerical model, see Supplemental Material, Sec. SI3 [60].

III. COMPUTATIONAL RESULTS AND DISCUSSION

The simulation is performed under the conditions described in Sec. II B for a STO single crystal of 3.5 μm length. Such a length might be the typical grain size in polycrystalline material. Surface exchange reactions of the oxygen and the cation sublattice according to Eqs. (14) and (15) are considered to be instantaneous at $T = 1500\,\mathrm{K}$, as mentioned above. The concentration of O vacancies, Sr vacancies, and electrons, as well as the space charge, the electric field, and the potential, are calculated for nonequidistant time increments until the new equilibrium is reached. Diffusion coefficients, mobilities, mass action constants, and dielectric permittivity are taken from the literature.

As we shall discuss in more detail, three time regimes [situations (i)–(iii) in Sec. II A] can be distinguished because of the orders of magnitude differences in the mobilities of the very fast electrons, the moderately fast O vacancies, and the very slow Sr vacancies. We discuss these three time regimes in Secs. A, B, and C below.

A. Equilibration of the electrons

After the pO_2 jump from 10^{-10} to 10^5 Pa at $T = 1500\,\mathrm{K}$, the new surface concentrations of electrons, O vacancies, and Sr vacancies are established instantaneously, according to the mass action laws. In particular, the new equilibrium at the surface at higher oxygen partial pressure implies a strong decrease in electron concentration and in oxygen vacancy concentration and an increase in Sr vacancy concentration [cf. Fig. 2(a)].

At this initial moment, the surface and bulk exhibit local electroneutrality at every position. The high mobility of the electrons ($0.28\,\mathrm{cm^2\,V^{-1}\,s^{-1}}$; Table I) immediately leads to a diffusion of electrons from the bulk towards the surface because of the high concentration gradient. This leads in turn to a depletion of electrons in the bulk near the surface and the formation of a positive space charge region due to the now unbalanced donor charges. The surface concentration of electrons increases during this process. Unexpectedly (in the classical picture), the surface concentration of Sr vacancies also starts to rise significantly, as the ratio $[V''_{Sr}]_{surf}/n^2_{surf}$ is forced to remain constant according to the surface equilibrium, Eq. (14).

The electronic equilibration process reaches a quasi-stationary state when the diffusion current of electrons towards the surface is equal to the drift current of electrons towards the bulk, induced by the electric field generated by the positive space charge of the donors. This space charge formation lowers the gradient in the electrons' electrochemical potential, canceling in the quasi-stationary state. In our simulations, the electronic equilibrium is established after some tens of picoseconds. Figure 3 shows the situation after the electronic equilibration at $t = 100\,\mathrm{ps}$ after the pO_2 jump.

As shown in Fig. 3(a), the surface concentration of Sr vacancies at $T = 1500\,\mathrm{K}$ is drastically enhanced ($\approx 3 \times 10^{21}\,\mathrm{cm^{-3}}$) compared with the new equilibrium value [$\approx 8 \times 10^{19}\,\mathrm{cm^{-3}}$, Fig. 2(a)] at the final pO_2 ($= 10^5$ Pa). Classically, surface concentrations may only vary between old and new equilibrium values. This classical picture, as we see here, is not always correct. Accordingly, the negative surface charge created by this classically unexpected excess of Sr vacancies as majority carriers strongly enhances the positive space charge (Fig. 3d).

Because of the reaction in Eq. (1), the O vacancies also show a surface concentration [$\approx 3 \times 10^{14}\,\mathrm{cm^{-3}}$, Fig. 3(b)] that differs from the new equilibrium value ($\approx 1 \times 10^{16}\,\mathrm{cm^{-3}}$). Hence, while the Sr vacancy concentration at the surface exceeds the new equilibrium value, the oxygen vacancy concentration is by more than one order of magnitude lower than the new equilibrium value. In this sense, we can regard the surface as *overoxidized* in this initial process. The electron density profile and the corresponding profiles of the space charge $\rho(x)$, the inner field $E(x)$, and electric potential $\varphi(x)$ are given in Figs. 3(c)–3(f), respectively. Here, we chose $\varphi = 0$ in the bulk.

The electron density profile in this quasi-equilibrium established within this short 100-ps time scale is given by the Boltzmann equation

$$n(x) = n_{\mathrm{bulk}} \cdot \exp\left(\frac{e_0\varphi(x)}{k_B T}\right), \tag{16}$$

where the potential profile $\varphi(x)$ enters in the exponent. Note, however, that the presented profiles are the result of our *dynamic* simulation—here performed in the picosecond time range.

The space charge formation yields a depletion of electrons and thus an insulating surface layer, already on this short time scale ($t = 100\,\mathrm{ps}$). The space charge region extends some nanometers into the bulk, corresponding to the Mott-Schottky screening length of the material. At the surface, the electron concentration is reduced by more than two orders of magnitude [Fig. 3(c)]. The initial oxidation process thus corresponds to an almost instantaneous MIT in the near-surface region. In fact, our simulation reveals an abrupt change of the near-surface electron concentration, which is only limited by the formation kinetics of cation vacancies at the surface.

On this short time scale, no inward diffusion of Sr vacancies is observed, in agreement with a classical estimation of the diffusion length ($L_D < 1$ Å). The corresponding depth profile is a steplike function [Fig. 3(a)]. For oxygen vacancies, one can classically estimate a diffusion length of about 1 nm. However, as shown in Fig. 3(b), the oxygen vacancy profile already bends downwards within the first 10 nm of the surface. This increase of the diffusion length on a small time scale is attributed to the electric field [$\approx 2.2\,\mathrm{MV\,cm^{-1}}$; Fig. 3(e)] in the electron depletion space charge layer near the surface, which is established immediately after the pO_2 jump and which accelerates the oxygen vacancy migration towards the surface. At the surface, a steep steplike decrease occurs, resulting from the fast surface reaction.

B. Equilibration of the O sublattice

The second time regime investigated in detail (up to milliseconds) is determined by the moderately fast migration of O vacancies, finally resulting in a quasi-equilibration of the O sublattice. In this time regime, the diffusion of Sr vacancies

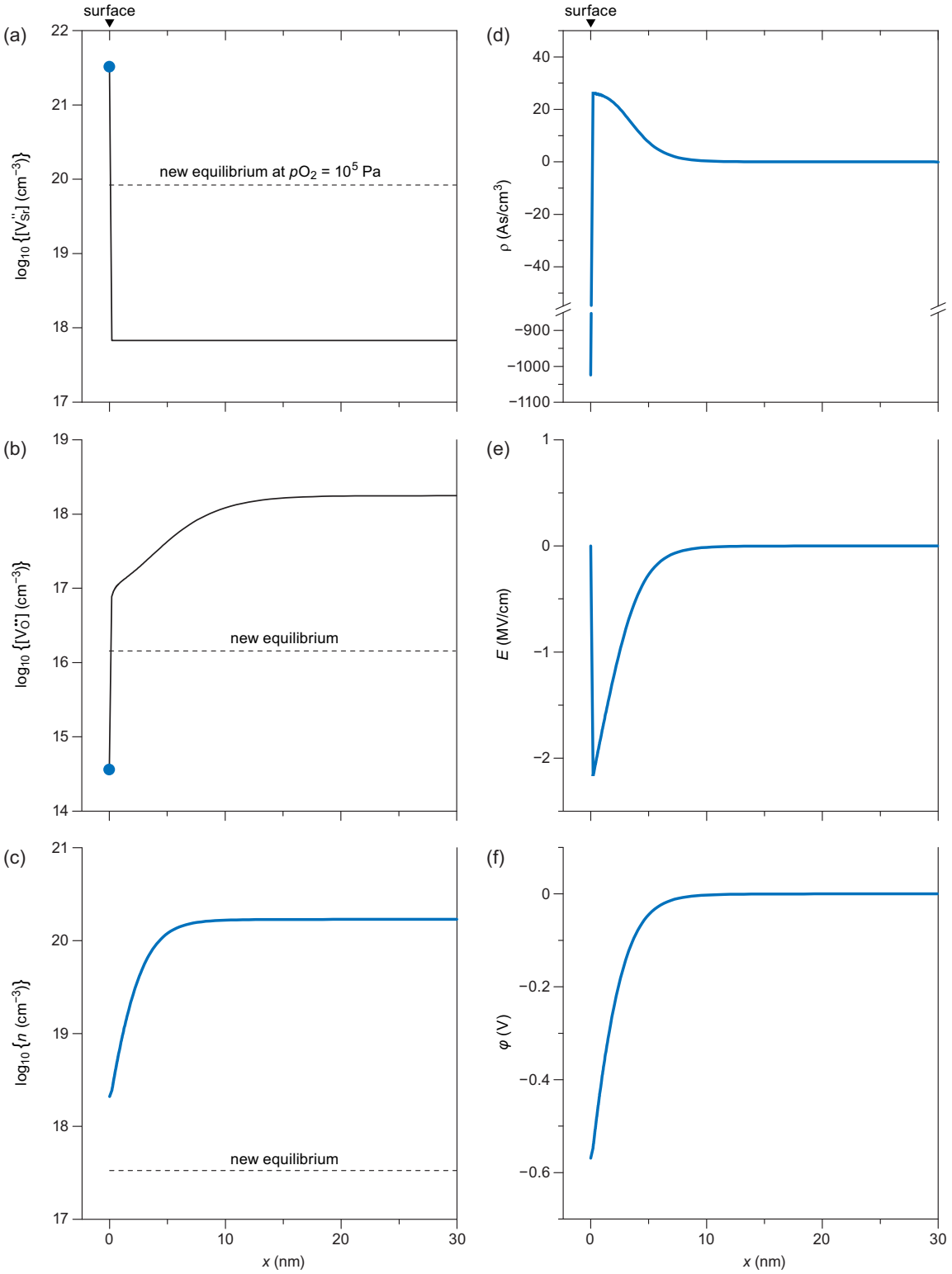

FIG. 3. Calculated electronic equilibrium at $t = 100$ ps [time range (i)] after a pO_2 jump from 10^{-10} to 10^5 Pa at 1500 K for 1 at % donor-doped $SrTiO_3$. The surface concentration of all species is assumed to react instantaneously. On this time scale, the electron density profile reaches a quasi-equilibrium. (a) Sr vacancy concentration, showing a very pronounced overshoot beyond the equilibrium value at the surface. (b) O vacancy concentration profile near the surface. (c) Electron density profile responsible for the generation of the depletion space charge region near the surface. (d) Space charge profile showing a negative charge density of $-1000\,As\,cm^{-3}$ in the surface layer because of the excess Sr vacancies at the surface, and a compensating positive space charge with a characteristic depth of approximately 5 nm. (e) Electric field E and (f) electric potential φ.

into the bulk is still negligible. Because O vacancies are minority carriers, they do not have any significant contribution to the space charge: Therefore, the charge density profile, the electric field, and the electrical potential in the SCR are mainly unaffected by this process and remain constant until the Sr vacancies have started to migrate significantly (see Sec. C). In particular, the ionized Nb-dopants ($1.6 \times 10^{20}\,\mathrm{cm}^{-3}$) provide the positive space charge in the SCR rather than the local concentration of mobile oxygen vacancies ($<2 \times 10^{18}\,\mathrm{cm}^{-3}$ at all x). Consequently, the electron depletion profile remains stationary, too, and the dynamics of the oxygen vacancy concentration profile is the only relevant process in this time scale. Therefore, after the establishment of the electronic equilibrium (Sec. III A), the subsequent out-diffusion of O vacancies from the bulk towards the surface takes place under a *stationary* electric field.

The results of our dynamic simulation in the intermediate time range are presented in Fig. 4. It shows the time evolution of the $[V_O^{\cdot\cdot}]$ profiles during the equilibration process from $t = 0$ to $t = 5\,\mathrm{ms}$. The colored plots refer to logarithmic time steps. Significant migration of oxygen vacancies is observed on the time scale of nanoseconds to milliseconds.

On a linear scale [Fig. 4(a)], the profiles appear to represent typical diffusion profiles. At $t = 1\,\mu\mathrm{s}$, the oxygen vacancy profile is about 300 nm wide (dark green line). In contrast to the short time range ($t = 100\,\mathrm{ps}$), this value now is in better agreement with the classical diffusion length, because outside the electron depletion layer at the surface, the ambipolar diffusion coefficient of O vacancies and electrons is approximately equal to the self-diffusion coefficient of the O vacancies due to the high concentration and mobility of the electrons.

However, there are some notable aspects arising from a more detailed inspection of the profiles. The logarithmic scale [Fig. 4(b)] shows that the value in the interior of the bulk approaches extraordinarily small values (approximately $6 \times 10^{10}\,\mathrm{cm}^{-3}$). This bulk value is four orders of magnitude lower than the initial concentration established at the already overoxidized surface. If we now magnify the region close to the surface [Fig. 4(c)], we observe an unexpected *enrichment* of O vacancies towards the surface. Such a concentration profile decaying into the bulk would naively be expected only during a *reduction* process. Contrary to expectation, the model thus predicts an *uphill diffusion* of oxygen vacancies during the *oxidation* process.

After approximately 5 ms (see Fig. 4), a quasi-equilibrium of the oxygen sublattice is reached. $[V_O^{\cdot\cdot}](x)$ can then be described by the potential profile $\varphi(x)$ with the Boltzmann equation

$$[V_O^{\cdot\cdot}](x) = [V_O^{\cdot\cdot}]_{\mathrm{surf}} \cdot \exp\left(\frac{2e_0(\varphi_{\mathrm{surf}} - \varphi(x))}{k_B T}\right). \qquad (17)$$

The surface concentration of O vacancies ($[V_O^{\cdot\cdot}]_{\mathrm{surf}} \approx 2 \times 10^{14}\,\mathrm{cm}^{-3}$) corresponds to the value calculated from Eq. (15). The extremely low value $[V_O^{\cdot\cdot}] \approx 6 \times 10^{10}\,\mathrm{cm}^{-3}$ in the interior of the crystal is thus determined by the electric field in the space charge layer at the surface driving the O vacancies towards the surface. The value is even lower than the O equilibrium value at $pO_2 = 10^5\,\mathrm{Pa}$ expected for an entirely frozen-in Schottky equilibrium (see Supplemental Material SI4 [60]).

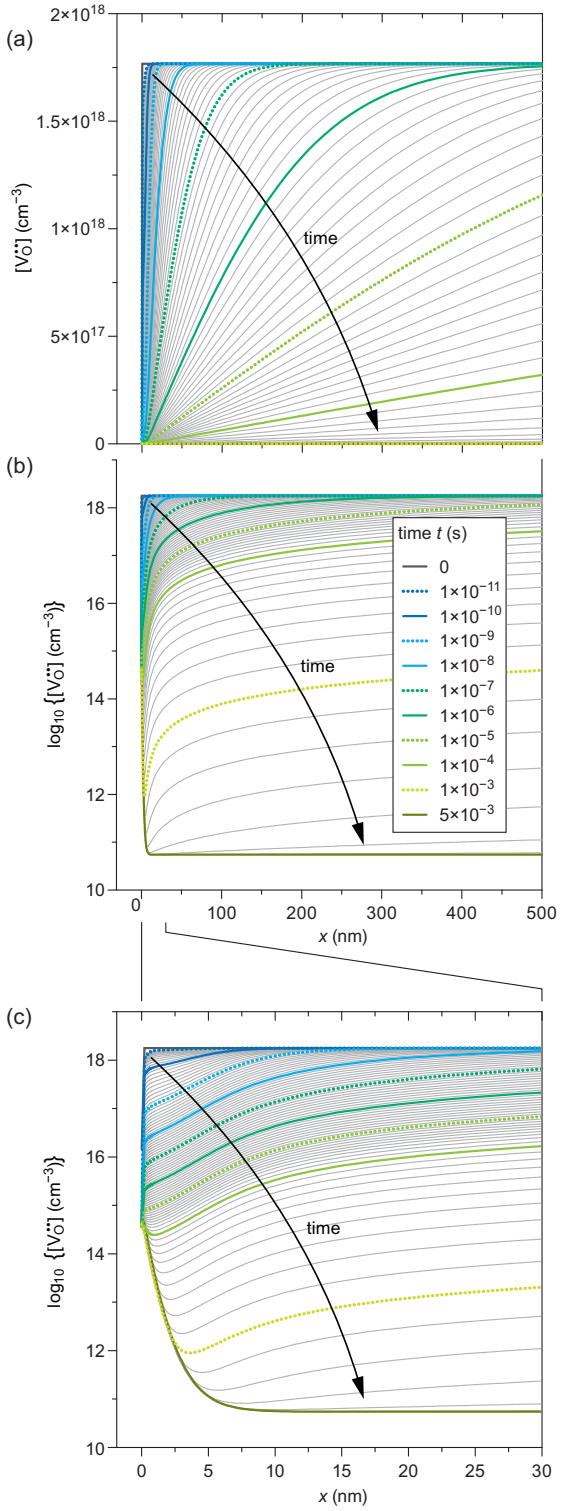

FIG. 4. Calculated equilibration of the O sublattice after a pO_2 jump from 10^{-10} to 10^5 Pa at 1500 K for 1 at % donor-doped $SrTiO_3$. The time evolution of the O vacancy density is shown on a linear scale (a), on a log scale (b), and on a log scale magnifying the region up to 30 nm from the surface. On the log scale, the unusual evolution of the concentration profiles due to the near-surface space charge is revealed. A time range of $t = 0$ to $t = 5 \times 10^{-3}\,\mathrm{s}$ is displayed, referring to time range (ii) in the main text. The colored lines mark logarithmic time increments. The quasi-equilibrium of the oxygen sublattice is reached after about 5 ms.

We explain this unexpected result with the presence of the strong electric field formed at the surface. On the one hand, the (low) concentration gradient of oxygen vacancies from the bulk towards the surface region causes (small) diffusion currents. On the other hand, the high negative internal electric field drives the oxygen vacancies further towards the surface, despite the opposite concentration gradient at the surface. As a result, oxygen vacancies accumulate in the near-surface region. The behavior of the oxygen vacancy concentration profile in this state of the oxidation process is highly unusual and solely caused by the surface space charge formation. While this behavior has only a minor impact on the electrical properties of *n*-STO (as oxygen vacancies are minority charge carriers), the uphill diffusion process is essential for understanding, e.g., oxygen ion diffusion in *n*-STO [46].

C. Equilibration of the Sr sublattice

The third time regime is determined by the slow motion of the Sr vacancies finally resulting in the equilibration of the Sr sublattice. This final state then corresponds to the new thermodynamic equilibrium of lattice disorder at the new pO_2 throughout the entire single crystal [cf. Fig. 2(a)]. Because Sr vacancies are majority carriers, their motion strongly influences the space charge region and, as a consequence, the electric field and potential. As we shall see, the space charge profile changes continuously, as it spreads out into the bulk and becomes less pronounced in its amplitude. Finally, it will disappear completely. The concentration profiles of electrons and the O vacancies will follow quasi-instantaneously. This is because the quasi-equilibria [Eqs. (16) and (17)] are rapidly reached on the time scale discussed in this section. In the course of the equilibration of the Sr vacancy profile, the initial surface excess of Sr vacancies decreases and finally vanishes.

Figure 5 shows the time evolution (100 μs to 10^6 s) of the concentration profiles of (a) Sr vacancies, (b) electrons, and (c) O vacancies, as well as the profiles of the space charge (d), the inner electric field (e), and the electric potential (f). Figure 6 displays enlarged views on the near-surface region. In our dynamical simulation, we observe the first significant migration of Sr vacancies at a simulation time of about 10 ms [Figs. 5(a) and 6(a)].

Classically, one would estimate a diffusion length of about 1 Å (migration over a distance of less than one lattice parameter) for Sr vacancies at 10 ms. However, our simulations reveal that the diffusion front has already reached about 1 nm (dark yellow line). This indicates that initially the Sr diffusion is (about a hundred times) faster than classically expected, as the diffusion process is accelerated by the initially strong electric field in the SCR.

A new equilibrium in the Sr sublattice, corresponding to a flat concentration profile at $[V''_{Sr}] \approx 8 \times 10^{19}\,\mathrm{cm}^{-3}$, is achieved after 10^6 s (∼10 d). This long-scale behavior is again in accordance with the self-diffusion coefficient for Sr vacancies at $T = 1500\,\mathrm{K}$ [$L_D(10^6\,\mathrm{s})$ is in the micrometer range, cf. Table I). This is because the field acceleration diminishes in the course of time, as shown in Fig. 5(e).

The density profiles of Sr vacancies and electrons *do not* show the typical shape of an error function (indicative of a diffusion process driven by concentration gradients only). Instead, an unusually shaped and pronounced diffusion front is observed. This is also a result of the time evolution of the electric field acting on the motion of the species in addition to the diffusion.

In terms of our simulation, these features on the long time scale can be regarded as an effect of a density-dependent ambipolar diffusion coefficient of the two majority carriers, electrons, and Sr vacancies, which varies with position and time: (1) *Ahead* of the diffusion front, the density of electrons exceeds the density of Sr vacancies by several orders of magnitude, so that the ambipolar diffusion coefficient in this region is given by the self-diffusion coefficient of Sr vacancies. (2) *Behind* the diffusion front, the charge balance mechanism of the donor charge changes from the electronically charge-balanced to Sr vacancy charge-balanced, i.e., $n \ll [V''_{Sr}]$. As a consequence, the ambipolar diffusion coefficient becomes significantly larger than the self-diffusion coefficient of Sr vacancies. This is a result of the negative electric field (Fig. 5e) accelerating the (negatively charged) Sr vacancies in this region, in particular, in the initial state.

In the course of time, both the electron concentration profile [Fig. 5(b)] and the oxygen vacancy profile [Fig. 5(c)] follow the Sr diffusion front, because of their quasi-equilibrium states achieved on these larger time scales. The quasi-equilibrium of the oxygen sublattice causes a widening of the unusual concentration profile. The electron concentration shows a depth profile inverse to the Sr vacancy profile. As a result, the electron depletion layer rapidly formed after the pO_2 jump grows into the bulk at the same speed as the Sr vacancy diffusion front. Hence, we observe a slow transition from the highly conducting electron charge-balanced *n*-STO to the insulating vacancy-compensated *n*-STO in the bulk.

Another remarkable feature is the evolution of the *surface concentrations* of all defects during the equilibration process as indicated by the arrows in Figs. 6(a)–6(c). As discussed above, the initial concentration of the majority defect, Sr vacancies, is found to be more than a factor of 40 larger than the new Schottky equilibrium value. This surface excess diminishes over time, as the defect profile widens into the bulk [Fig. 6(a)]. At the same time, the surface concentration of electrons decreases as a result of the quasi-equilibrium [Fig. 6(b)]. In contrast, the oxygen vacancy concentration *increases* again upon oxidation [Fig. 6(c)]. Hence, after the initial fast drop of the oxygen vacancy concentration to very small values in the bulk (Sec. III B), the *oxidation* process involves the *formation* of oxygen vacancies on this time scale. This an unexpected and nonintuitive result. The reason is the decrease of the surface Sr vacancy concentration and the initial overoxidation of surface and bulk driven by the quasi-equilibrium of the oxygen sublattice. In the course of time, the O vacancies hence start to diffuse back into the bulk, following the in-diffusion of Sr vacancies, and finally approach the equilibrium value given in Fig. 2(a).

As mentioned, the origin of the variation of the surface concentrations with time is of similar nature as the acceleration of the diffusion of Sr vacancies, namely the formation of a kinetic space charge layer between surface and diffusion front. The highest local space charge is found at the surface. This causes a widening of the Sr vacancy profile and a subsequent shift in the surface concentrations. In total, this leads to an

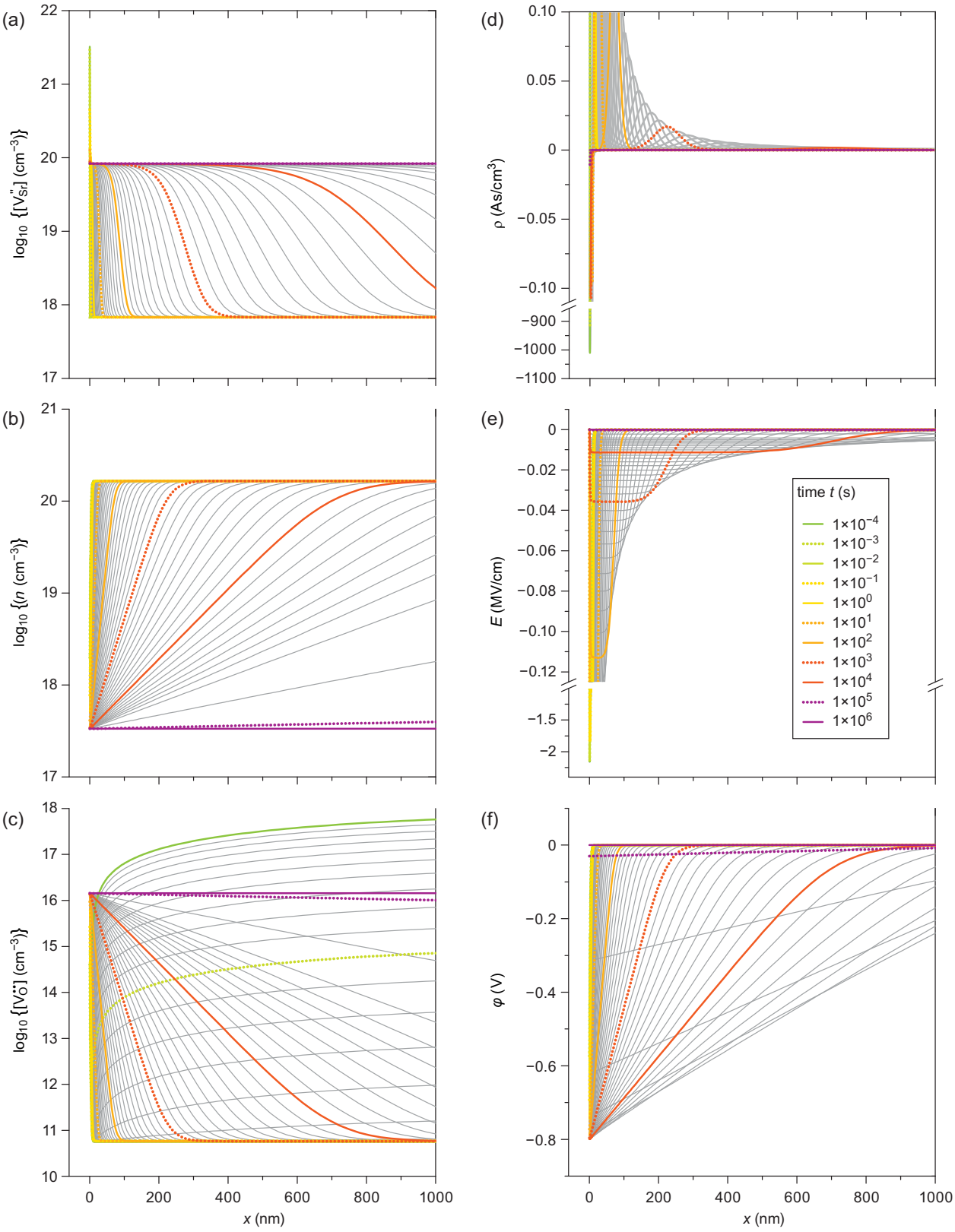

FIG. 5. Calculated equilibration of the Sr sublattice after a pO_2 jump from 10^{-10} to 10^5 Pa at 1500 K for 1 at % donor-doped $SrTiO_3$. (a) Time evolution of the Sr vacancy density for $t = 10^{-4}$ s to $t = 10^6$ s, referring to time range (iii) in the main text. (b) Time evolution of the electron density showing how the metal-insulation transition driven by in-diffusion of Sr vacancies proceeds into the bulk. (c) Time evolution of the O vacancy density illustrating the increase in oxygen vacancy concentration after the very strong initial depression (cf. Fig. 4). (d–f) Shows time evolution of the space charge density, the electric field, and the electrostatic potential, respectively.

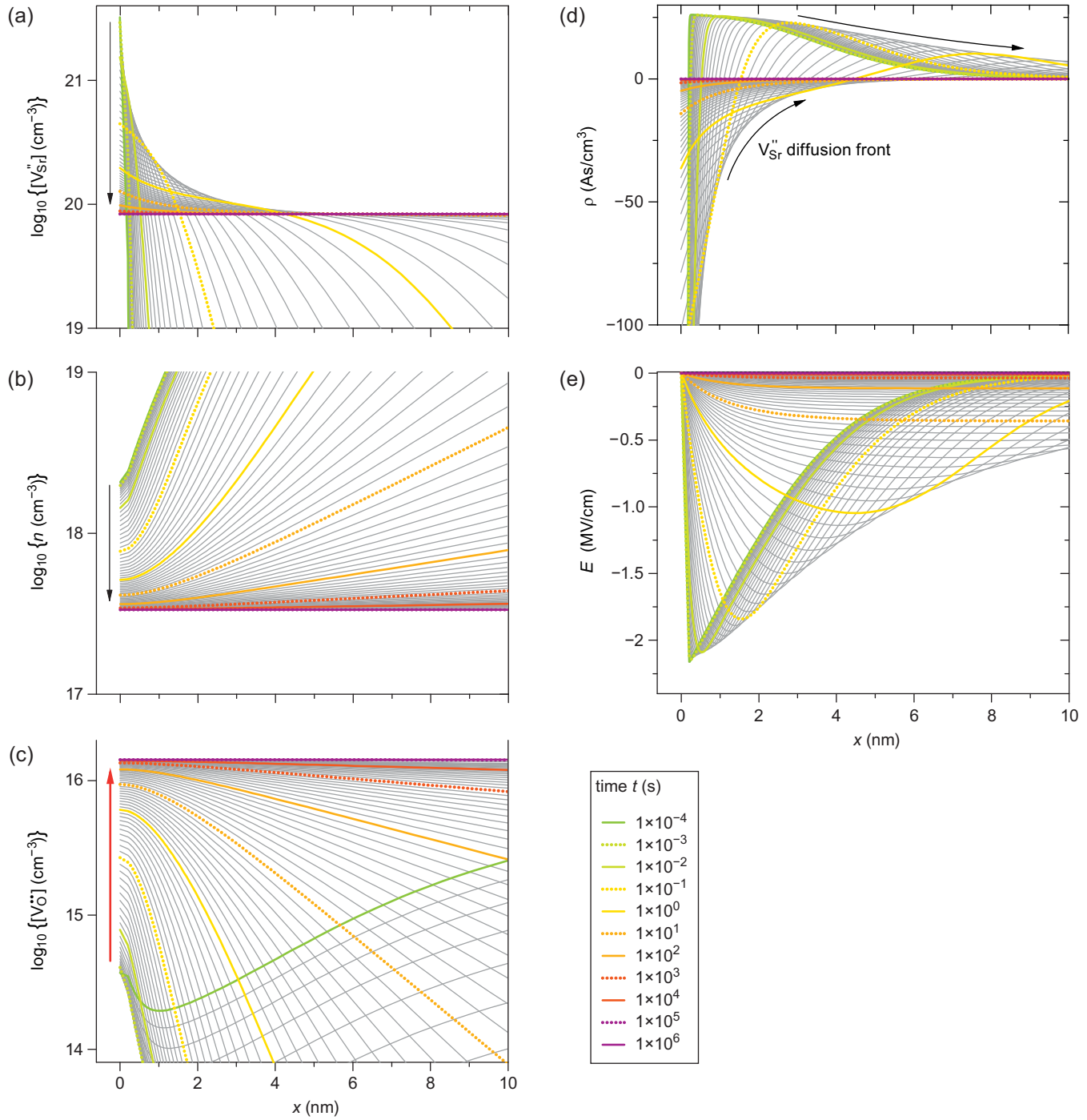

FIG. 6. Time evolution of defect concentrations, electric field, and charge density in the near-surface region ($0 < x\,(\text{nm}) < 10$) on time scale (iii), $t = 10^{-4}$ s to $t = 10^{6}$ s. (a) Illustrates the decrease of the excess surface concentration of Sr vacancies in the course of time, (b) the decrease in electron concentration, and (c) the unusual *increase* in oxygen vacancy concentration after the initial overoxidation illustrated in Fig. 4.

overall increase of the total Sr vacancy concentration within the space charge layer and thus the negative charge density near the surface. At the same time, the surface density of electrons within the surface layer reduces, until a new local equilibrium is established. In the course of time (10^5–10^6 s), the surface space charge [Fig. 6(d)] diminishes, and the associated field [Fig. 6(e)] as well as its effect on the surface concentrations becomes less pronounced.

The surface concentrations as well as the bulk concentrations ($x = 1.75\,\mu$m) of all species as a function of time are displayed in Fig. 7(a). One can distinguish the three time scales (i), (ii), and (iii) discussed above. The partial equilibrium of the electronic subsystem (i) is reached almost instantaneously ($t \sim 10^{-10}$ s). The initial surface concentration of electrons (dark red line) being much lower than the bulk concentration (light red) corresponds to the formation of the electron

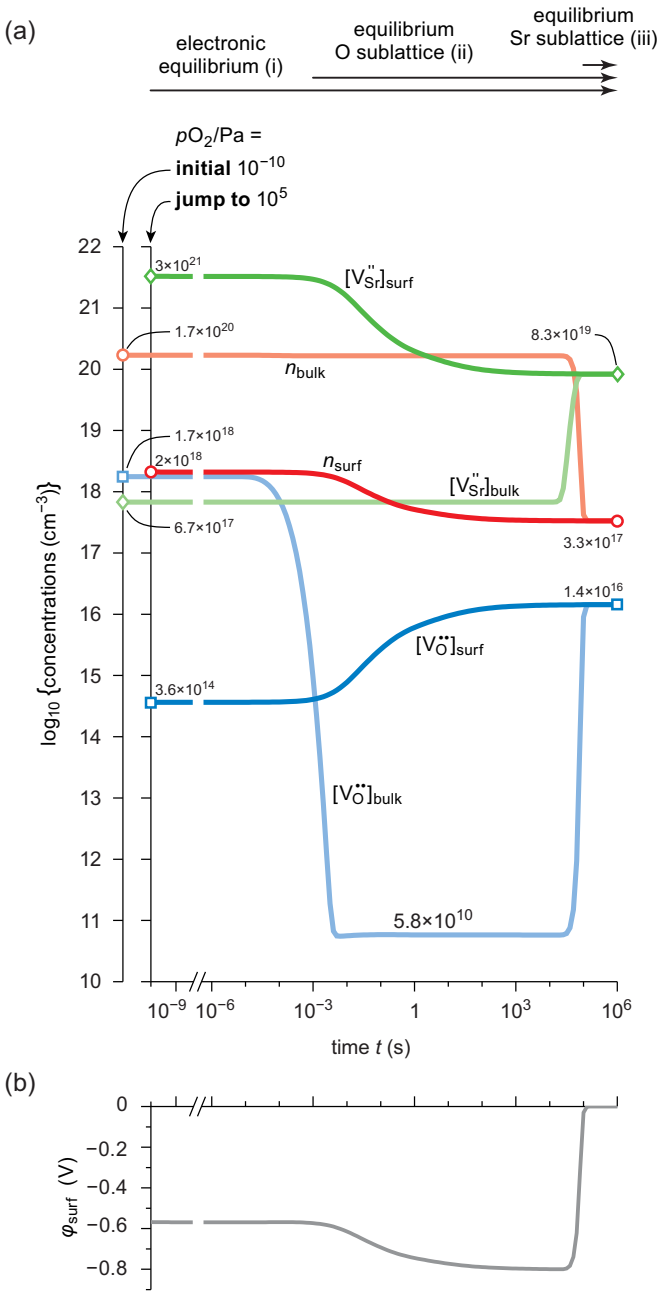

FIG. 7. Summary of the calculated concentrations (a) and the electrostatic potential at the surface (b) over all three time regimes. (a) The concentrations of Sr vacancies (green), electrons (red), and O vacancies (blue) are shown for the surface (dark colors) and for the bulk (at depth 1.75 μm, light colors).

depletion layer. The partial equilibrium of the oxygen sublattice (ii) is reached after a few milliseconds, as indicated by the huge drop in the bulk concentration of oxygen vacancies (light blue line). This drop of the bulk concentration well below the surface concentration (dark blue line) represents the effect of uphill diffusion revealed on this time scale. Finally, the equilibrium of the Sr sublattice (green lines), and thus the equilibrium state of the entire system, is achieved after 1–10 d; here, surface defect concentrations and bulk concentrations are identical.

As illustrated in Fig. 7, the effect of time-dependent surface densities of Sr vacancies also does not only exist at very short times but remains present for several hours (dark green line) under the chosen oxidation conditions.

On short time scales, the high (excess) concentration of Sr vacancies at the very near surface causes an initial surface potential of −0.57 V. The in-diffusion of Sr vacancies is associated with a slow increase of the surface potential to −0.80 eV. Only at very long times does the potential fall to zero [see Fig. 7(b)]. The evolution of the surface potential barrier can therefore be broken down in three stages. The first stage is given by the reaction rate of Sr vacancies at the surface and the space charge formation described in Sec. III A. The second stage is then dominated by the kinetics of the cation sublattice, i.e., the in-diffusion of Sr vacancies. The final stage corresponds to the sample approaching the new equilibrium ($\varphi \rightarrow 0$).

IV. IMPACT OF SPACE CHARGE FORMATION ON THE ELECTRICAL RESPONSE OF *n*-STO

The formation of the kinetic SCR upon oxidation has a tremendous effect on the electronic response of *n*-STO, in particular that of the surface. Based on our simulation results, we are able to provide qualitative predictions for the different time scales, allowing us to revisit experimental findings reported in the literature. In fact, our model suggests an extremely rapid MIT in the near-surface region of *n*-STO, which is much more pronounced than predicted in the classical picture, followed by a very slow MIT moving into the bulk of the material in the course of the oxidation process.

The electron depletion layer formed immediately after exposure to oxidizing conditions [time scale (i), Fig. 3] corresponds to a potential barrier (∼0.6 eV) for electron transport across the surface space charge layer. Due to the carrier depletion, electron transport along the surface of *n*-STO is suppressed immediately after oxygen exposure, too. Hence, at the surface, one already expects band bending and a rapid MIT upon oxidation in the very initial phase of the oxidation process, in which only negligible inward diffusion of Sr vacancies occurs.

For in-plane conduction measurements on single crystals, this has only a limited effect, as the insulating surface region is electrically shorted by the still highly conducting bulk. For thin films, however, the effect of the surface space charge layer is more severe, as electrons may be depleted from the entire thin film. As shown in Ref. [89], *n*-STO thin films grown at considerably oxidizing conditions and/or annealed in high oxygen pressure can be insulating—even though they contain large amounts of shallow donor dopants. They show conduction only above a critical thickness that relates to the Debye screening length of the deposited thin film, indicating a surface space charge effect, rather than a growth-related effect. In Ref. [89], this behavior was assigned to surface states and a resulting surface pinning potential of about 0.7 eV (at 5 at % La doping), which is in remarkably good agreement with the surface potentials obtained in our simulations (Fig. 3). Hence, the observed thickness effect in *n*-STO thin films indicates that surface Sr vacancy-driven space charge formation is already effective at $T \approx 1000$ K, i.e., at a much lower temperature than

examined in this paper. In our model, band bending occurs due to the annihilation of electrons and the formation of acceptors (Sr vacancies) at the surface according to Eqs. (5) and (14). These acceptors are fully ionized under all conditions we have simulated, i.e., the Fermi level stays sufficiently high so that these acceptors do not trap holes. Therefore, Sr vacancies at the surface of *n*-STO can be regarded as giving rise to extrinsic acceptor-type surface states [90].

Note that electron depletion is not observed in delta-doped structures in which the *n*-doped STO layer is covered by an additional undoped top layer before a postannealing process in oxidizing conditions is performed [91,92]. In this case, Sr vacancy formation in the buried *n*-STO layer would require significant diffusion of Sr towards the surface and is, therefore, sluggish and can be suppressed by limiting the annealing time. As a result, delta-doped structures stay conducting also for a thickness of the *n*-doped layer well below its Debye screening length.

The space charge formation as described in this paper is also expected to affect the electronic band structure at interfaces between *n*-STO substrates and a functional thin film grown on top of it. As has been shown by electron holography, surprisingly significant band bending occurs on the *n*-STO substrate side of epitaxial Nb:STO/Fe:STO heterostructures [20]. In order to reproduce the measured potential characteristics across the structure, interfacial acceptor-type defect states had to be assumed. Here, the band bending on the Nb:STO side of the interface is found to be about 0.6 V, and the total concentration of interfacial acceptor states corresponds to $4 \times 10^{20}\,\mathrm{cm}^{-3}$ distributed over about 4 unit cells of the *n*-STO substrate (approximately equivalent to $1.6 \times 10^{21}\,\mathrm{cm}^{-3}$ acceptors confined to a single unit cell). Both values, converted into concentrations of Sr vacancies, are in good agreement with our calculations. Note that before thin film deposition, *n*-STO substrates are commonly annealed in air or oxygen flow at temperatures of about 950–1000 °C for a few hours (i.e., time scales (i)–(iii) depending on temperature) to achieve a defined step terrace structure desired for epitaxial growth [93]. According to our study, the surface of such a treated substrate will be electron-depleted as a result of the surface oxidation and will thus show intrinsic band bending towards the surface. Thus, we can again conclude that the interfacial acceptor states proposed in Ref. [20] are in actual fact Sr vacancies formed at the substrate's surface prior to thin film deposition.

Such results emphasize the importance of the detailed understanding of the oxidation process in *n*-STO for all thin-film studies performed on *n*-STO substrates. In fact, a similar electron-depleted SCR has to be considered for *any* *n*-STO substrate after applying an annealing process in oxygen-rich atmospheres. In this view, the large negative trap charge promoting stable resistive switching at the interface between Pt and *n*-STO [26] may be related to Sr vacancy accumulation at the interface, too.

Additionally, according to our model, polycrystalline (i.e., ceramic) samples are expected to show an immediate increase in electrical resistance upon oxidation, as the potential barriers established at the grain boundaries form a network of additional serial resistances. On short time scales, the bulk of each grain is still highly conducting, so electrons can travel freely once they have passed the surface potential barrier (∼5–10 nm, cf. Fig. 3). However, as the oxidation process proceeds in the course of time, the electron depletion layer widens, and the height of the potential barrier increases to about 0.8 eV as a result of Sr vacancy diffusion [time scale (iii), Figs. 5,7]. Hence, the immediate increase in resistance is followed by a slower, gradual increase in resistance, and hence a slow MIT in the bulk. Such a behavior of the electrical resistance at high temperature has indeed been observed for *n*-STO [47], as well as *n*-BTO [73,94–104] ceramics.

V. SUMMARY AND CONCLUSION

The present paper reports on the MIT in donor-doped $SrTiO_3$ (*n*-STO) upon oxidation driven by a large change in the oxygen partial pressure at elevated temperatures. Using an implicit finite differences approach, the motion of all defects is calculated on the basis of a continuous medium model. In contrast to earlier models, we consider a global charge neutrality condition instead of a local one, in order to accommodate the interactions of ionic defects with the intrinsic internal electric field formed during the oxidation process. This approach allows for the formation of *kinetically controlled space charge layers* at the surface evolving during the equilibration process due to the different diffusion coefficients of the species involved. In return, this leads to time variant surface defect concentrations.

If the oxygen partial pressure is changed instantaneously from reducing condition (electronically charge-balanced) to oxidizing (cation vacancy charge-balanced) conditions at high temperatures, the kinetic model discloses a threefold re-equilibration process of (1) the electronic band structure, (2) the oxygen sublattice, and (3) the cation sublattice taking place on very different time scales. The main results of our study can be summarized as follows.

(i) On the short-term scale (up to 100 ps), the establishment of the electronic equilibria yields a rapid formation of an electron depletion SCR and a corresponding potential barrier at the surface. The SCR formation is driven by the fast formation of Sr vacancies only in the surface layer, while there is no *diffusion* of Sr vacancies into the bulk.

(ii) Because of the active surface equilibrium reaction during the SCR formation, the Sr vacancy surface density exceeds the new equilibrium by more than one order of magnitude. We call this effect an "overoxidation."

(iii) As a result of overoxidation, the SCR is much more pronounced than in the classical model. This is associated with a correspondingly enhanced drop in the conductivity and thus a particularly pronounced MIT in the near-surface region.

(iv) On the midterm scale (up to a few milliseconds), the equilibration of the oxygen sublattice takes place. The electron depletion profile as well as the electrical properties of the material do not change during this process, since the O vacancies are minority carriers.

(v) Driven by the strong internal electric field in the SCR, O vacancies are enriched in the near-surface region on the midterm scale. Oxygen vacancies are forced to move against their concentration gradient, so that the profile reveals an anomalous "uphill diffusion" shape, in agreement with ^{18}O diffusion data reported in the literature.

(vi) On the long time scale (up to days), the equilibration process is dominated by the defect kinetics of the Sr sublattice. The initial surface excess of Sr vacancies fades while the width of the SCR increases along with the diffusion front of the Sr vacancy profile. The amplitude of the SCR decreases until it completely vanishes in the end. The electron density profile, as well as the O vacancy profile, can be regarded as being in quasi-equilibrium states, dictated by the slowly evolving Sr vacancy profile.

(vii) Initially, the strong electric field in the SCR accelerates the (very slow) Sr vacancy diffusion by a factor of about 100. This field acceleration vanishes as the SCR fades in the course of time.

The formation of the pronounced electron depletion SCR at the surface of *n*-STO and the local equilibration of the cation sublattice imply severe consequences for the electrical properties of *n*-STO thin films and the interfacial band structure in epitaxial thin-film devices based on *n*-STO substrates. In particular, the effects of surface carrier depletion and concentration profiles, as well as interface bend banding, may be seen from a different perspective, now considering the near-surface and near-interface lattice disorder of *n*-STO as discussed in this paper. Based on this model, the understanding of the resistive switching behavior of *n*-STO, as well as the strategies to tailor electronic properties of *n*-STO thin films and interfaces, may be refined. The model may also contribute to a link between the macroscopic understanding of the dynamics of the lattice disorder and surface structures observed on the atomistic level after dedicated surface treatments. Moreover, the processes described by the model will help to refine the understanding of the formation of grain boundary potential barriers in donor-doped ceramics, such as PTCRs (positive temperature coefficient of resistance), resistive sensors, and internal boundary layer capacitors.

The presented model is not limited to the investigated material but might describe a general mechanism, which can be found in a variety of different ionic materials with similar lattice disorder.

ACKNOWLEDGMENT

Assistance in the numerical simulation by Stephan Menzel is highly appreciated. This paper was supported in part by the Deutsche Forschungsgemeinschaft (DFG) through SFB 917.

[1] D. G. Schlom and J. Mannhart, Oxide electronics: Interface takes charge over Si, Nat. Mater. **10**, 168 (2011).

[2] A. P. Ramirez, Oxide electronics emerge, Science **315**, 1377 (2011).

[3] D. G. Schlom, L.-Q. Chen, X. Pan, A. Schmehl, and M. A. Zurbuchen, A thin film approach to engineering functionality into oxides, J. Am. Ceram. Soc. **91**, 2429 (2008).

[4] H. Y. Hwang, Y. Iwasa, M. Kawasaki, B. Keimer, N. Nagaosa, and Y. Tokura, Emergent phenomena at oxide interfaces, Nat. Mater. **11**, 103 (2012).

[5] A. F. Santander-Syro, O. Copie, T. Kondo, F. Fortuna, S. Pailhes, R. Weht, X. G. Qiu, F. Bertran, A. Nicolaou, A. Taleb-Ibrahimi, P. Le Fevre, G. Herranz, M. Bibes, N. Reyren, Y. Apertet, P. Lecoeur, A. Barthelemy, and M. J. Rozenberg, Two-dimensional electron gas with universal subbands at the surface of SrTiO(3), Nature **469**, 189 (2011).

[6] A. F. Santander-Syro, F. Fortuna, C. Bareille, T. C. Rödel, G. Landolt, N. C. Plumb, J. H. Dil, and M. Radovic, Giant spin splitting of the two-dimensional electron gas at the surface of $SrTiO_3$, Nat. Mater. **13**, 1085 (2014).

[7] S. Kowalczyk, F. Mcfeely, L. Ley, V. Gritsyna, and D. Shirley, The electronic structure of $SrTiO_3$ and some simple related oxides (MgO, Al_2O_3, SrO, TiO2), Solid State Commun. **23**, 161 (1977).

[8] A. Spinelli, M. A. Torija, C. Liu, C. Jan, and C. Leighton, Electronic transport in doped $SrTiO_3$: Conduction mechanisms and potential applications, Phys. Rev. B **81**, 155110 (2010).

[9] H. P. R. Frederikse and W. Hosler, Hall mobility in $SrTiO_3$, Phys. Rev. **161**, 822 (1967).

[10] G. M. Choi, H. L. Tuller, and D. Goldschmidt, Electronic-transport behavior in single-crystalline $Ba_{0.03}Sr_{0.97}TiO_3$, Phys. Rev. B **34**, 6972 (1986).

[11] R. Moos and K. H. Haerdtl, Electronic transport properties of $Sr_{1-x}La_xTiO_3$ ceramics, J. Appl. Phys. **80**, 393 (1996).

[12] T. A. Cain, A. P. Kajdos, and S. Stemmer, La-doped $SrTiO_3$ films with large cryogenic thermoelectric power factors, Appl. Phys. Lett. **102**, 182101 (2013).

[13] Y. Kozuka, Y. Hikita, C. Bell, and H. Y. Hwang, Dramatic mobility enhancements in doped $SrTiO_3$ thin films by defect management, Appl. Phys. Lett. **97**, 012107 (2010).

[14] J. Son, P. Moetakef, B. Jalan, O. Bierwagen, N. J. Wright, R. Engel-Herbert, and S. Stemmer, Epitaxial $SrTiO_3$ films with electron mobilities exceeding 30,000 $cm^2\ V^{-1}\ s^{-1}$, Nat. Mater. **9**, 482 (2010).

[15] A. Verma, A. P. Kajdos, T. A. Cain, S. Stemmer, and D. Jena, Intrinsic Mobility Limiting Mechanisms in Lanthanum-Doped Strontium Titanate, Phys. Rev. Lett. **112**, 216601 (2014).

[16] T. Susaki, Y. Kozuka, Y. Tateyama, and H. Y. Hwang, Temperature-dependent polarity reversal in Au/Nb : $SrTiO_3$ Schottky junctions, Phys. Rev. B **76**, 155110 (2007).

[17] H. Inoue, A. G. Swartz, N. J. Harmon, T. Tachikawa, Y. Hikita, M. E. Flatté, and H. Y. Hwang, Origin of the Magnetoresistance in Oxide Tunnel Junctions Determined through Electric Polarization Control of the Interface, Phys. Rev. X **5**, 041023 (2015).

[18] Y. Hikita, K. Nishio, L. C. Seitz, P. Chakthranont, T. Tachikawa, T. F. Jaramillo, and H. Y. Hwang, Band edge engineering of oxide photoanodes for photoelectrochemical water splitting: Integration of subsurface dipoles with atomic-scale control, Adv. Energy Mater. **6**, 1502154 (2016).

[19] R. Schafranek, S. Payan, M. Maglione, and A. Klein, Barrier height at (Ba,Sr)TiO3/Pt interfaces studied by photoemission, Phys. Rev. B **77**, 195310 (2008).

[20] A. Marchewka, D. Cooper, C. Lenser, S. Menzel, H. Du, R. Dittmann, R. E. Dunin-Borkowski, and R. Waser,

Determination of the electrostatic potential distribution in Pt/Fe:$SrTiO_3$/Nb:$SrTiO_3$ thin-film structures by electron holography, Sci. Rep. **4**, 6975 (2014).

[21] T. Okuda, K. Nakanishi, S. Miyasaka, and Y. Tokura, Large thermoelectric response of metallic perovskites: Sr1-xLaxTiO3 ($0 < -x < -0.1$), Phys. Rev. B **63**, 113104 (2001).

[22] A. Kinaci, C. Sevik, and T. Cagin, Electronic transport properties of $SrTiO_3$ and its alloys: $Sr_{1-x}La_xTiO_3$ and $SrTi_{1-x}M_xO_3$ (M = Nb, Ta), Phys. Rev. B **82**, 155114 (2010).

[23] K. Ozdogan, M. U. Kahaly, S. R. S. Kumar, H. N. Alshareef, and U. Schwingenschlögl, Enhanced carrier density in Nb-doped $SrTiO_3$ thermoelectrics, J. Appl. Phys., **111**, 054313 (2012).

[24] T. Fujii, M. Kawasaki, A. Sawa, H. Akoh, Y. Kawazoe, and Y. Tokura, Hysteretic current-voltage characteristics and resistance switching at an epitaxial oxide Schottky junction $SrRuO_3/SrTi_{0.99}Nb_{0.01}O_3$, Appl. Phys. Lett. **86**, 012107 (2005).

[25] C. Rodenbücher, W. Speier, G. Bihlmayer, U. Breuer, R. Waser, and K. Szot, Cluster-like resistive switching of $SrTiO_3$:Nb surface layers, New J. Phys. **15**, 103017 (2013).

[26] E. Mikheev, B. D. Hoskins, D. B. Strukov, and S. Stemmer, Resistive switching and its suppression in Pt/Nb:$SrTiO_3$ junctions, Nat. Commun. **5**, 3990 (2014).

[27] J. G. Bednorz and K. A. Muller, Perovskite-type oxides-the new approach to high-T_c superconductivity, Rev. Mod. Phys. **60**, 585 (1988).

[28] D. Olaya, F. Pan, C. T. Rogers, and J. C. Price, Superconductivity in La-doped strontium titanate thin films, Appl. Phys. Lett. **84**, 4020 (2004).

[29] J. Yin, J. Ye, and Z. Zou, Enhanced photoelectrolysis of water with photoanode Nb:SrTiO_3, Appl. Phys. Lett. **85**, 689 (2004).

[30] M. Yang, L. Z. Ren, Y. J. Wang, F. M. Yu, M. Meng, W. Q. Zhou, S. X. Wu, and S. W. Li, Direct evidences of filamentary resistive switching in Pt/Nb-doped $SrTiO_3$ junctions, J. Appl. Phys., **115**, 134505 (2014).

[31] C. Baeumer, N. Raab, T. Menke, C. Schmitz, R. Rosezin, P. M. Müller, M. Andrä, V. Feyer, R. Bruchhaus, F. Gunkel, C. M. Schneider, R. Waser, and R. Dittmann, Verification of redox-processes as switching and retention failure mechanisms in Nb:$SrTiO_3$/metal devices, Nanoscale **8**, 13967 (2016).

[32] A. Sawa, T. Fujii, M. Kawasaki, and Y. Tokura, Highly rectifying $Pr_{0.7}Ca_{0.3}MnO_3/SrTi_{0.9998}Nb_{0.0002}O_3$ p-n junction, Appl. Phys. Lett. **86**, 112508 (2005).

[33] T. Fujii, M. Kawasaki, A. Sawa, Y. Kawazoe, H. Akoh, and Y. Tokura, Electrical properties and colossal electroresistance of heteroepitaxial $SrRuO_3/SrTi_{1-x}Nb_xO_3$ ($0.0002 \leqslant x \leqslant 0.02$) Schottky junctions, Phys. Rev. B **75**, 165101 (2007).

[34] E. Mikheev, J. Hwang, A. P. Kajdos, A. J. Hauser, and S. Stemmer, Tailoring resistive switching in $\{Pt\}/\{SrTiO\}_3$ junctions by stoichiometry control, Sci. Rep. **5**, 11079 (2015).

[35] L. L. Hench and J. K. West, *Principles of Electronic Ceramics* (Wiley, New York, 1990).

[36] C. Baeumer, C. Schmitz, A. H. H. Ramadan, H. Du, K. Skaja, V. Feyer, P. Muller, B. Arndt, C. Jia, J. Mayer, R. A. De Souza, C. Michael Schneider, R. Waser, and R. Dittmann, Spectromicroscopic insights for rational design of redox-based memristive devices, Nat. Commun. **6**, 8610 (2015).

[37] R. Muenstermann, T. Menke, R. Dittmann, and R. Waser, Coexistence of filamentary and homogeneous resistive switching in Fe-doped $SrTiO_3$ thin-film memristive devices, Adv. Mater. **22**, 4819 (2010).

[38] C. Lenser, M. Patt, S. Menzel, A. Köhl, C. Wiemann, C. M. Schneider, R. Waser, and R. Dittmann, Insights into nanoscale electrochemical reduction in a memristive oxide: The role of three-phase boundaries, Adv. Funct. Mater. **24**, 4466 (2014).

[39] V. Garcia and M. Bibes, Ferroelectric tunnel junctions for information storage and processing, Nature Communications **5**, 4289 (2014).

[40] T. Susaki, N. Nakagawa, and H. Y. Hwang, Transport mechanisms in manganite-titanate heterojunctions, Phys. Rev. B **75**, 104409 (2007).

[41] R. Moos and K. H. Härdtl, Defect chemistry of donor-doped and undoped strontium titanate ceramics between 1000 °C and 1400 °C, J. Am. Ceram. Soc. **80**, 2549 (1997).

[42] D. M. Smyth, *The Defect Chemistry of Metal Oxides* (Oxford University Press, New York, 2000).

[43] K. Gomann, G. Borchardt, M. Schulz, A. Gomann, W. Maus-Friedrichs, B. Lesage, O. Kaitasov, S. Hoffmann-Eifert, and T. Schneller, Sr diffusion in undoped and La-doped $SrTiO_3$ single crystals under oxidizing conditions, Phys. Chem. Chem. Phys. **7**, 2053 (2005).

[44] R. A. De Souza, Oxygen diffusion in $SrTiO_3$ and related perovskite oxides, Adv. Funct. Mater. **25**, 6326 (2015).

[45] K. Szot, W. Speier, U. Breuer, R. Meyer, J. Szade, and R. Waser, Formation of micro-crystals on the (100) surface of $SrTiO_3$ at elevated temperatures, Surf. Sci. **460**, 112 (2000).

[46] R. Meyer, R. Waser, J. Helmbold, and G. Borchardt, Observation of Vacancy Defect Migration in the Cation Sublattice of Complex Oxides by ^{18}O Tracer Experiments, Phys. Rev. Lett. **90**, 105901 (2003).

[47] W. Menesklou, H. Schreiner, K. H. Härdtl, and E. Ivers-Tiffée, High temperature oxygen sensors based on doped $SrTiO_3$, Sens. Actuators B: Chem. **59**, 184 (1999).

[48] F. Gunkel, P. Brinks, S. Hoffmann-Eifert, R. Dittmann, M. Huijben, J. E. Kleibeuker, G. Koster, G. Rijnders, and R. Waser, Influence of charge compensation mechanisms on the sheet electron density at conducting $LaAlO_3/SrTiO_3$-interfaces, Appl. Phys. Lett. **100**, 052103 (2012).

[49] F. Gunkel, R. Waser, A. H. H. Ramadan, R. A. De Souza, S. Hoffmann-Eifert, and R. Dittmann, Space charges and defect concentration profiles at complex oxide interfaces, Phys. Rev. B **93**, 245431 (2016).

[50] J. Crawford and P. Jacobs, Point defect energies for strontium titanate: A pair-potentials study, J. Solid State Chem. **144**, 423 (1999).

[51] M. J. Akhtar, Z.-U.-N. Akhtar, R. A. Jackson, and C. R. A. Catlow, Computer simulation studies of strontium titanate, J. Am. Ceram. Soc. **78**, 421 (1995).

[52] F. A. Kröger and H. J. Vink, Relations between the concentrations of imperfections in crystalline solids, Solid State Phys. **3**, 307 (1956).

[53] R. Meyer, R. Waser, J. Helmbold, and G. Borchardt, Cationic surface segregation in donor-doped $SrTiO_3$ under oxidizing conditions, J. Electroceram. **9**, 101 (2002).

[54] B. Rahmati, J. Fleig, W. Sigle, E. Bischoff, J. Maier, and M. Rühle, Oxidation of reduced polycrystalline Nb-doped $SrTiO_3$: Characterization of surface islands, Surf. Sci. **595**, 115 (2005).

[55] Z. Wang, X. Hao, S. Gerhold, M. Schmid, C. Franchini, and U. Diebold. Vacancy clusters at domain boundaries and band bending at the $SrTiO_3$(110) surface, Phys. Rev. B, **90**, 035436 (2014).

[56] S. Gerhold, Z. Wang, M. Schmid, and U. Diebold, Stoichiometry-driven switching between surface reconstructions on $SrTiO_3$(001), Surf. Sci. **621**, L1 (2014).

[57] M. S. J. Marshall, D. T. Newell, D. J. Payne, R. G. Egdell, and M. R. Castell, Atomic and electronic surface structures of dopants in oxides: STM and XPS of Nb- and La-doped $SrTiO_3$(001), Phys. Rev. B **83**, 035410 (2011).

[58] R. A. De Souza, V. Metlenko, D. Park, and T. E. Weirich, Behavior of oxygen vacancies in single-crystal $SrTiO_3$: Equilibrium distribution and diffusion kinetics, Phys. Rev. B **85**, 174109 (2012).

[59] M. Schie, R. Waser, and R. A. De Souza, A simulation study of oxygen-vacancy behavior in strontium titanate: Beyond nearest-neighbor interactions, J. Phys. Chem. C **118**, 15185 (2014).

[60] See Supplemental Material at http://link.aps.org/supplemental/10.1103/PhysRevB.94.115408 for details on cation diffusivity in STO (SI1), temperature dependence of defect concentrations in bulk *n*-STO (SI2), computational methods (SI3), and bulk defect concentration in the quenched state (SI4).

[61] Rotraut Merkle and Joachim Maier, How Is oxygen incorporated into oxides? A comprehensive kinetic study of a simple solid-state reaction with $SrTiO_3$ as a model material, Angew. Chem. Int. Ed. **47**, 3874 (2008).

[62] T. Bieger, J. Maier, and R. Waser, Kinetics of oxygen incorporation in $SrTiO_3$ (Fe-doped): An optical investigation, Sens. Actuators B **B7**, 763 (1992).

[63] H.-J. Hagemann and H. Ihrig, Valence change and phase stability of 3d-doped BaTi03 annealed in oxygen and hydrogen, Phys. Rev. B **20**, 3871 (1979).

[64] A. Rothschild, W. Menesklou, H. L. Tuller, and E. Ivers-Tiffée, Electronic structure, defect chemistry, and transport properties of $SrTi_{1-x}Fe_xO_{3-y}$ solid solutions, Chem. Mater. **18**, 3651 (2006).

[65] C. R. Song and H. I. Yoo, Chemical diffusivity of $BaTiO_{3-\delta}$: Defect chemical analysis, Phys. Rev. B **61**, 3975 (2000).

[66] R. Waser and R. Hagenbeck, Grain boundaries in dielectric and mixed-conducting ceramics, Acta Mater. **48**, 797 (2000).

[67] R. Waser, Bulk conductivity and defect chemistry of acceptor-doped strontium titanate in the quenched state, J. Am. Ceram. Soc. **74**, 1934 (1991).

[68] J. Daniels, Defect equilibria in acceptor-doped barium-titanate, Philips Res. Rep. **31**, 505 (1976).

[69] R. A. De Souza, F. Gunkel, S. Hoffmann-Eifert, and R. Dittmann, Finite-size versus interface-proximity effects in thin-film epitaxial $SrTiO_3$, Phys. Rev. B **89**, 241401(R) (2014).

[70] R. A. De Souza, The formation of equilibrium space-charge zones at grain boundaries in the perovskite oxide $SrTiO_3$, Phys. Chem. Chem. Phys. **11**, 9939 (2009).

[71] R. Hagenbeck and R. Waser, Influence of temperature and interface charge on the grain-boundary conductivity in acceptor-doped $SrTiO_3$ ceramics, J. Appl. Phys. **83**, 2083 (1998).

[72] H. M. Chan, M. P. Harmer, and D. M. Smyth, Compensating defects in highly donor-doped $BaTiO_3$, J. Am. Ceram. Soc. **69**, 507 (1986).

[73] R. Wernicke, The influence of kinetic processes on the electrical conductivity of donor-doped batio3 ceramics, Phys. Status Solidi A **47**, 139 (1978).

[74] J. Daniels and K. H. Haerdtl, Electrical-conductivity at high-temperatures of donor-doped barium-titanate ceramics, Philips Res. Rep. **31**, 489 (1976).

[75] C. Lee, J. Destry, and J. L. Brebner, Optical absorption and transport in semiconducting $SrTiO_3$, Phys. Rev. B **11**, 2299 (1975).

[76] These values refer to bulk values that have been determined in various independent measurements at zero or low fields. They do not inherently include any dependence on the (local) electric field.

[77] L. Aballe, S. Matencio, M. Foerster, E. Barrena, F. Sanchez, J. Fontcuberta, and C. Ocal, Instability and surface potential modulation of self-patterned (001)$SrTiO_3$ surfaces, Chem. Mater. **27**, 6198 (2015).

[78] R. Bachelet, F. Sanchez, J. Santiso, C. Munuera, C. Ocal, and J. Fontcuberta, Self-assembly of $SrTiO_3$(001) chemical-terminations: A route for oxide-nanostructure fabrication by selective growth, Chem. Mater. **21**, 2494 (2009).

[79] C. Wagner, Beitrag zur Theorie des Anlaufsvorgangs, Z. Phys. Chemie **B21**, 25 (1933).

[80] S. M. Sze and Kwok K. Ng, *Physics of Semiconductor Devices* (Wiley, New York, 2007).

[81] J. Maier, *Physical Chemistry of Ionic Materials* (Wiley, New York, 2004).

[82] A. Mueller and K. Haerdtl, Ambipolar diffusion phenomena in BaTiO3 and $SrTiO_3$, Appl. Phys. A **49**, 75 (1989).

[83] J. Philibert, *Atom Movements—Diffusion and Mass Transport in Solids*, Monographies de Physique (Editions de Physique, Les Ulis, France, 1991).

[84] D. Poetzsch, R. Merkle, and J. Maier, Stoichiometry variation in materials with three mobile carriers—Thermodynamics and transport kinetics exemplified for protons, oxygen vacancies, and holes, Adv. Funct. Mater. **25**, 1542 (2015).

[85] D.-K. Lee and H.-I. Yoo. Unusual oxygen re-equilibration kinetics of TiO2-d, Solid State Ionics, **177**, 1 (2006).

[86] K.-H. Hellwege and A. M. Hellwege (Hrsg.), *Landolt-Börnstein, Zahlenwerte und Funktionen aus Naturwissenschaft und Technik, Gruppe I3: Kristall- und Festkörper, Band 16 erroelektrika und verwandte Substanzen, Teilband a* (Springer-Verlag, Berlin, 1981).

[87] R. C. Neville, B. Hoeneisen, and C. A. Mead, Permittivity of strontium titanate, J. Appl. Phys. **43**, 2124 (1972).

[88] R. Merkle, R. DeSouza, and J. Maier, Optically tuning the rate of stoichiometry changes: Surface-controlled oxygen incorporation into oxides under uv irradiation, Angew. Chem. Int. Ed. **40**, 2126 (2001).

[89] A. Ohtomo and H. Y. Hwang, Surface depletion in doped $SrTiO_3$ thin films, Appl. Phys. Lett. **84**, 1716 (2004).

[90] Frederick Seitz, Henry Ehrenreich, and David Turnbull, *Solid State Physics: Advances in Research and Applications* (Elsevier, 1974), p. 29.

[91] Y. Kozuka, M. Kim, C. Bell, B. G. Kim, Y. Hikita, and H. Y. Hwang, Two-dimensional normal-state quantum oscillations in a superconducting heterostructure, Nature **462**, 487 (2009).

[92] H. Inoue, M. Kim, C. Bell, Y. Hikita, S. Raghu, and H. Y. Hwang, Tunable coupling of two-dimensional superconductors

in bilayer $SrTiO_3$ heterostructures, Phys. Rev. B **88**, 241104 (2013).

[93] G. Koster, B. L. Kropman, G. J. H. M. Rijnders, D. H. A. Blank, and H. Rogalla, Quasi-ideal strontium titanate crystal surfaces through formation of strontium hydroxide, Appl. Phys. Lett. **73**, 2920 (1998).

[94] W. Preis and W. Sitte, Modelling of grain boundary resistivities of n-conducting BaTiO3 ceramics, Solid State Ionics **177**, 2549 (2006).

[95] Yet-Ming Chiang and Touichi Takagi, Grain-boundary chemistry of barium titanate and strontium titanate: I, high-temperature equilibrium space charge, J. Am. Ceram. Soc. **73**, 3278 (1990).

[96] W. Preis and W. Sitte, Modeling of electrical properties of grain boundaries in n-conducting barium titanate ceramics as a function of temperature and dc-bias, Solid State Ionics **262**, 486 (2014).

[97] T. Frömling, J. Hou, W. Preis, W. Sitte, H. Hutter, and J. Fleig, Oxygen tracer diffusion in donor doped barium titanate, J. Appl. Phys. **110**, 043531 (2011).

[98] W. Preis and W. Sitte, Electronic conductivity and chemical diffusion in n-conducting barium titanate ceramics at high temperatures, Solid State Ionics **177**, 3093 (2006).

[99] W. Preis, A. Bürgermeister, W. Sitte, and P. Supancic, Bulk and grain boundary resistivities of donor-doped barium titanate ceramics, Solid State Ionics **173**, 69 (2004).

[100] F. D. Morrison, A. M. Coats, D. C. Sinclair, and A. R. West, Charge compensation mechanisms in La-doped BaTiO3, J. Electroceram. **6**, 219 (2001).

[101] Finlay D. Morrison, Derek C. Sinclair, and Anthony R. West, Electrical and structural characteristics of lanthanum-doped barium titanate ceramics, J. Appl. Phys. **86**, 6355 (1999).

[102] S. R. Morrison, *Electrochemistry at Semiconductor and Oxidized Metal Electrodes* (Plenum Press, New York, 1980).

[103] F. Poignant, l'Oxydation de ceramiques a base de titanate de strontium semiconducteur et la formation de barriere de potentiel aux joints de grains, Ph.D. thesis, Umoges, France,1995.

[104] J. Maier, G. Schwitzgebel, and H. Hagemann, Electrochemical investigations of conductivity and chemical diffusion in pure and doped cubic $SrTiO_3$ and BaTiO3, J. Solid State Chem. **58**, 1 (1985).